



Assessing the reliability and consistency of InSAR and GNSS data for retrieving 3D-displacement rapid changes, the example of the 2015 Piton de la Fournaise eruptions



Aline Peltier ^{a,*}, Jean-Luc Froger ^b, Nicolas Villeneuve ^a, Thibault Catry ^c

^a Observatoire Volcanologique du Piton de la Fournaise, Institut de Physique du Globe de Paris, Sorbonne Paris Cité, Univ. Paris Diderot, CNRS, F-97418 La Plaine des Cafres, La Réunion, France

^b Université Clermont Auvergne - CNRS - IRD, OPGC, Laboratoire Magmas et Volcans, F-63000 Clermont-Ferrand France

^c ESPACE-DEV, UMR 228 IRD/UM/UR/UG/UA, Institut de Recherche pour le Développement (IRD), Maison de la Télédétection, 500 rue Jean-François Breton, F-34093 Montpellier Cedex 5, France

ARTICLE INFO

Article history:

Received 22 July 2016

Received in revised form 24 March 2017

Accepted 27 March 2017

Available online 29 March 2017

ABSTRACT

InSAR and GNSS are now the best and most developed techniques in the Earth sciences to track deformation, especially in volcanology. In this study, we assess the reliability and consistency of these two techniques for measuring 3-D ground displacements - and not only the displacement in the direction of the InSAR Line of Sight - on volcanoes during rapid changes. The use of a large amount of satellite data (X, C, L-band as well as right and left-looking acquisitions) made it possible to retrieve the 3-D displacement components with an unprecedented accuracy. We carry out this evaluation on the Piton de la Fournaise volcano, where four eruptions occurred in 2015. The comparison between GNSS and InSAR allows us: (i) to describe the deformation pattern associated with these eruptions, (ii) to quantify the discrepancies between InSAR and GNSS, and (iii) to discuss the limits and the complementarities of InSAR and GNSS. The ground deformation patterns associated with the four eruptions of Piton de la Fournaise in 2015 are typical of this volcano, with decimeter ground displacements asymmetrically distributed along the dike path, evidencing a preferential eastward motion, particularly visible thanks to the broad spatial coverage of InSAR. Except for the NS component, InSAR and GNSS data are in overall agreement, with most of the GNSS-InSAR residuals <2.5 cm and <5 cm on the EW and vertical component, respectively, i.e. within the error bar of the two methods. Most of the discrepancies on the terminal cone can be attributed to uncorrected atmospheric effects in InSAR. Our study confirms the consistency and the complementarity of the two methods to characterize (i) the 3-D ground deformation distribution in high spatial resolution (InSAR), and (ii) the dynamism (GNSS) associated with eruptive activity.

© 2017 Elsevier B.V. All rights reserved.

1. Introduction

Ground deformation monitoring in volcanic areas covers a broad range of techniques, with field (e.g., tiltmeters, extensometers, strainmeters, leveling), airborne (Structure from Motion photogrammetry), and spaceborne (Interferometric Synthetic Aperture Radar: InSAR) observations. The Global Navigation Satellite System (GNSS) is a hybrid method, based on both receivers in the field (ground segment) and on satellite constellations in space (satellite segment).

The first volcano ground deformation networks were implemented in the field (initially with leveling and tilt surveys, then with the installation of permanent stations; e.g. Jaggar and Finch, 1929; Wilson, 1935; Dzurisin et al., 2012). GNSS is now one of the most powerful tools installed in the field to detect subtle ground deformation and it is used worldwide to monitor volcanoes, especially on accessible and very

active edifices such as Etna (Italy), Kilauea (Hawai'i), and Piton de la Fournaise (La Réunion) for which continuous long time series are available (e.g. Owen et al., 2000; Houlié et al., 2006; Peltier et al., 2008; Aloisi et al., 2011; Poland et al., 2012; Staudacher and Peltier, 2016). Permanent GNSS stations allow continuous and real or near-real time monitoring, with precision and accuracy of a few mm, at defined and specific locations. By contrast, ground deformation measurements provided by space technology via InSAR are punctual in time (e.g. revisit period of 24 days for RADARSAT-2, 8 days for Cosmoskymed, 11 days for TerraSAR-X and 6 days for the Sentinel-1 constellations) but provide dense information on a large spatial scale (1 to tens or so of km²), with centimeter/millimeter-level accuracy. Following the technological advances and the major efforts made over the past few decades on processing chains, InSAR has become an essential tool to track deformation changes on active volcanoes (e.g. Massonnet et al., 1993; Massonnet and Feigl, 1998; Jonsson et al., 1999; Dzurisin, 2000; Froger et al., 2001, 2004; Yun et al., 2006; Wauthier et al., 2009; Pinel et al., 2011, 2014; Brunori et al., 2012; Catry et al., 2015).

* Corresponding author.

E-mail address: peltier@ipgp.fr (A. Peltier).

All these methods - in the field and from space - thus appear to be highly complementary in detecting and characterizing (i) the ground deformation distribution, and (ii) the dynamism associated with unrest and eruptive activity. With technological advancements, and the progressive development of these new techniques since the end of the 20th century, more and more data are now available. A lot of deformation studies performed on volcanoes are based on the joint studies and/or inversion of InSAR and GNSS data (e.g. Fernández et al., 2003; Palano et al., 2008; Jonsson, 2009; Sudhaus and Jonsson, 2009; Biggs et al., 2010; Peltier et al., 2010; Sigmundsson et al., 2010; Chadwick et al., 2011; Feigl et al., 2014; Parks et al., 2015; Sigmundsson et al., 2015). Only a few are focused on the cross evaluation (validity and limitations) of the methods in relation to each other to retrieve 3-D ground displacements (EW, NS, UP), as the comparison is usually performed in the InSAR Line of Sight direction. Indeed, retrieving 3-D ground displacements from InSAR requires the use of a large amount of SAR data acquired under various independent acquisition geometries, a condition rarely achieved.

Piton de la Fournaise (basaltic shield volcano, La Réunion Island, Indian Ocean), often considered as a volcano-laboratory, is an ideal target to develop such cross evaluation of 3-D displacement mapping thanks to: i) its high level of activity (mean of 1 eruption every 9 months over the last few decades; e.g. Peltier et al., 2009; Roult et al., 2012); ii) its large and dense in-situ monitoring network maintained by the volcanological observatory (Observatoire Volcanologique du Piton de la Fournaise; OVPF-IPGP); iii) its large cover by SAR satellite data (since the end of the 1990s, Piton de la Fournaise has been regularly imaged by RADARSAT-1 & -2, JERS-1, ENVISAT-ASAR, ALOS-PALSAR-1 & -2, TerraSAR-X and TanDEM-X, the four satellites of CSK constellation and Sentinel-1A and 1B); iv) the vegetation-free nature of surface material in the summit area of Piton de la Fournaise (Enclos Fouqué caldera and terminal cone, see location on Fig. 1), which ensures a good interferometric coherence and has allowed InSAR to be successfully developed since 1998 (e.g. Sigmundsson et al., 1999; Froger et al., 2004, 2015; Fukushima et al., 2005; Bato et al., 2016).

The specificity of this work is the comparison of the 3-D ground displacement results -and not only the displacement in the direction of the InSAR Line of Sight- coming from the InSAR and GNSS methods during rapid changes in volcanic area. This has been made possible by using a large amount of satellite data (X, C, L-band as well as right and left-looking acquisitions). We carried out this multi-sensor evaluation by assessing the rapid volcano deformation linked to the four eruptions that occurred in 2015 at Piton de la Fournaise (February 4–15; May 17–30; July 31–August 2; August 24–October 31, see locations on Fig. 1). These four eruptions, like 97% of the recent eruptive activity (Villeneuve & Bachèlery, 2006), were located inside the Enclos Fouqué caldera (Fig. 1). This study gives us a general overview of the reliability and consistency of these two methods for measuring 3-D ground displacements in volcanic areas during rapid changes.

2. Methods

2.1. InSAR

2.1.1. InSAR acquisition at Piton de la Fournaise

More than 1100 radar images have been acquired for Piton de la Fournaise by various Space Agencies since 1996, mainly at the request of the Indian Ocean InSAR Observatory Service (OI2) since 2003. OI2 is part of the National Service for Volcanological Observation of the French National Research Council Institute for Earth Sciences and Astronomy (CNRS/INSU). It is currently operated jointly by the Observatoire de Physique du Globe de Clermont-Ferrand and the Volcanological Observatory of Piton de la Fournaise. OI2's main tasks include ensuring that radar images are regularly taken over Piton de la Fournaise, producing interferograms from these images and making these interferograms available to the community through a dedicated web site (<https://www.obs.univ-bpclermont.fr/casoar>). In > 13 years of InSAR monitoring of Piton de la Fournaise carried out by OI2, 2015 was a particularly fruitful year, not only in terms of volcanic activity, but also in terms of amount and diversity of radar data acquired. Thus, all the four eruptions of 2015 were imaged with Cosmo-Skymed (X-band), Sentinel-1 (C-

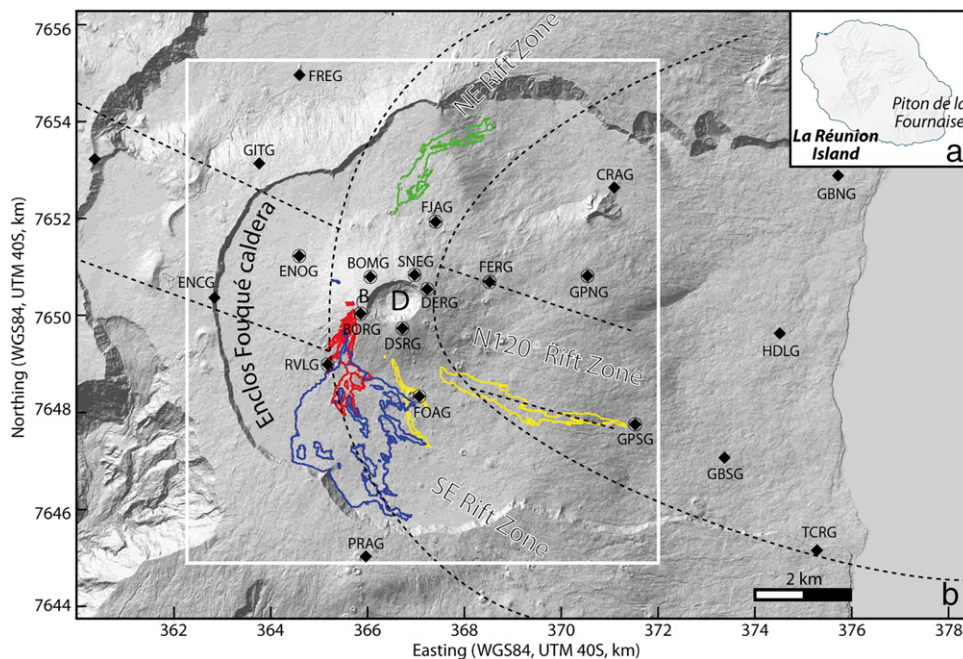


Fig. 1. Piton de la Fournaise setting. (a) Location of Piton de la Fournaise on La Réunion Island. (b) Shaded relief of the Piton de la Fournaise volcano with locations of the rift zones and the lava flows of February 4–15, 2015 (in red), May 17–30, 2015 (in yellow), July 31–August 2, 2015 (in green), and August 24–October 31, 2015 (in blue). Diamonds represent the locations of the OVPF permanent GNSS stations inside and close to the Enclos Fouqué caldera. The circled diamonds are the GNSS stations used in this study. “B” and “D” refer to the Bory and Dolomieu craters, respectively. The white square shows the area covered by this study. Coordinates in kilometers (WGS84, UTM 40S).

band) and ALOS-2 (L-band) data (with both right-looking and left-looking ALOS-2 data for the last three eruptions). In addition, the February and May eruptions were also imaged by TerraSAR-X/TanDEM-X (X-band) and RADARSAT-2 (C-band) data.

From these data, we were able to calculate, for each eruption, between 8 and 12 interferograms (Table 1; Fig. 2). The number of

interferograms covering a particular eruption is not only determined by the availability of SAR images acquired by the Space Agencies on the volcano during the eruption (more precisely, in the days or weeks preceding and following the eruption) but also by the lapse of time between two successive eruptions. For instance, the end of the July eruption and the beginning of the August eruption were separated by only

Table 1

Summary of the InSAR data available for the computation of displacement maps associated with the four dike injections of February, May, July and August 2015. Data in italic were not used in the displacement inversion procedure. Light gray highlights data that are redundant, in terms of acquisition geometry, and that were averaged before being used in the displacement component inversion procedure. Maximum and minimum extreme dates are highlighted in bold. ^aCSK = Cosmo-Skymed; TSX/TDX = TerraSAR-X/TanDEM-X; RS2 = RADARSAT-2; S1A = Sentinel-1A. ^bAcquisition Mode: SM = Stripmap; IW = Interferometric Wide Swath; SM1 = Stripmap 1 for ALOS2; SPT = Spotlight. ^cR = Range; A = Azimuth. ^dLD = Looking Direction; A = Ascending; D = Descending; R = right; L = Left. ^eRadarlook is determined for the Piton de la Fournaise summit. It does not change significantly on the whole area affected by the displacement pattern of the four 2015 eruptions.

Satellite ^a	Band	Acq. mode ^b	Resolution R/A ^c (m)	Beam	Pass LD ^d	LOS unit vector ^e			Date master yyyy/mm/dd	Date slave yyyy/mm/dd	Variance (10 ⁻³ m ²)
						EW	NS	UD			
February Eruption, 2015/02/04 – 2015/02/15											
CSK	X	SM	1.63/2.25	HI_15	AR	-0.73	-0.18	0.66	2014/12/24	2015/02/10	6.6
CSK	X	SM	1.74/2.10	HI_18	DR	0.77	-0.20	0.61	2014/12/24	2015/03/30	2.1
CSK	X	SM	1.74/2.10	HI_18	DR	0.77	-0.20	0.61	2015/01/17	2015/02/10	2.1
CSK	X	SM	1.18/2.10	HI_05	DR	0.56	-0.13	0.82	2015/01/23	2015/02/09	1.4
TSX/TDX	X	SM	1.36/1.87	008	AR	-0.54	-0.12	0.83	2015/01/20	2015/02/11	5.5
TSX/TDX	X	SM	1.36/1.87	010	DR	0.59	-0.13	0.80	2014/10/06	2015/03/09	2.1
RS2	C	SM	4.73/4.80	Q27	AR	-0.69	-0.19	0.70	2014/10/08	2015/02/05	7.7
RS2	C	SM	4.73/4.80	Q28	DR	0.71	-0.19	0.68	2014/10/10	2015/02/07	14.7
S1A	C	IW	2.33/14.07	151	DR	0.58	-0.14	0.80	2015/01/20	2015/03/09	
S1A	C	IW	2.33/14.07	151	DR	0.58	-0.14	0.80	2015/02/01	2015/03/21	
ALOS2	L	SPT	1.43/0.97	168	AR	-0.79	-0.21	0.58	2015/01/23	2015/02/06	8.6
ALOS2	L	SM1	1.43/1.95	59	DR	0.67	-0.16	0.73	2015/01/24	2015/03/07	7.2
May Eruption, 2015/05/17 – 2015/05/30											
CSK	X	SM	1.63/2.25	HI_15	AR	-0.73	-0.18	0.66	2015/05/17	2015/05/25	5.1
CSK	X	SM	1.74/2.10	HI_18	DR	0.77	-0.20	0.61	2015/02/10	2015/05/17	3.4
CSK	X	SM	1.74/2.10	HI_18	DR	0.77	-0.20	0.61	2015/03/30	2015/05/25	3.4
TSX/TDX	X	SM	1.36/1.87	008	AR	-0.54	-0.12	0.83	2015/05/10	2015/06/01	14.5
TSX/TDX	X	SM	1.36/1.87	010	DR	0.59	-0.13	0.80	2015/05/14	2015/06/05	8.2
RS2	C	SM	4.73/4.80	Q8	AR	-0.46	-0.11	0.88	2015/05/09	2015/06/02	13.4
S1A	C	SM	3.19/4.11	144	AR	-0.66	-0.17	0.73	2015/05/07	2015/05/19	3.3
S1A	C	SM	2.66/4.15	151	DR	0.58	-0.14	0.80	2015/05/08	2015/05/20	3.5
ALOS2	L	SPT	1.43/0.97	170	AR	-0.88	-0.25	0.40	2015/04/27	2015/05/25	241.8
ALOS2	L	SPT	1.43/0.97	162	AL	0.46	0.09	0.89	2015/04/29	2015/06/10	54.2
ALOS2	L	SPT	1.43/0.97	158	AL	0.89	0.14	0.44	2015/05/07	2015/06/04	51.8
July Eruption, 2015/07/31 – 2015/08/02											
CSK	X	SM	1.63/2.25	HI_15	AR	-0.73	-0.18	0.66	2015/07/28	2015/08/13	9.9
S1A	C	SM	2.33/14.07	144	AR	-0.66	-0.17	0.73	2015/07/06	2015/08/11	5.2
S1A	C	SM	2.33/14.07	151	DR	0.58	-0.14	0.80	2015/06/25	2015/08/12	128.6
ALOS2	L	SM1	1.43/1.95	59	DR	0.67	-0.16	0.73	2015/07/11	2015/08/22	16.4
ALOS2	L	SPT	1.43/0.97	170	AR	-0.88	-0.25	0.40	2015/05/25	2015/08/03	22.6
ALOS2	L	SPT	1.43/0.97	160	AL	0.76	0.13	0.64	2015/07/12	2015/08/23	14.9
ALOS2	L	SPT	1.43/0.97	158	AL	0.89	0.14	0.44	2015/06/18	2015/08/13	19.3
ALOS2	L	SPT	1.43/0.97	66	DL	-0.78	0.14	0.61	2015/07/15	2015/08/15	15.0
August Eruption, 2015/08/24 – 2015/10/31											
CSK	X	SM	1.63/2.25	HI_15	AR	-0.73	-0.18	0.66	2015/08/13	2015/09/02	6.7
CSK	X	SM	1.63/2.25	HI_15	AR	-0.73	-0.18	0.66	2015/08/13	2015/09/14	6.7
S1A	C	SM	2.33/14.07	144	AR	-0.66	-0.17	0.73	2015/08/23	2015/09/28	11.3
S1A	C	SM	2.33/14.07	151	DR	0.58	-0.14	0.80	2015/08/12	2015/11/16	3.2
ALOS2	L	SM1	1.43/1.95	59	DR	0.67	-0.16	0.73	2015/08/22	2015/10/03	8.7
ALOS2	L	SM1	1.43/1.95	60	DR	0.52	-0.12	0.83	2015/08/13	2015/09/24	18.8
ALOS2	L	SPT	1.43/0.97	159	AL	0.84	0.14	0.53	2015/08/04	2015/10/13	33.2
ALOS2	L	SPT	1.43/0.97	66	DL	-0.78	0.14	0.61	2015/08/15	2015/08/29	28.6

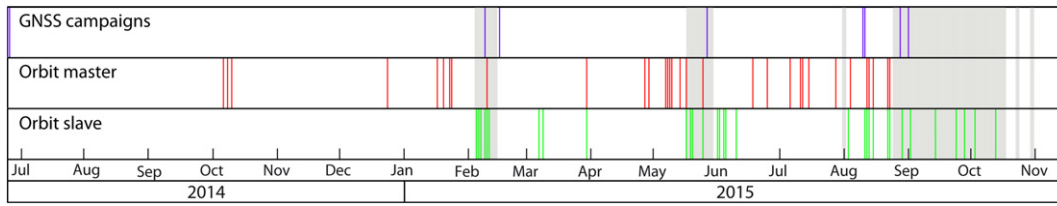


Fig. 2. Chronogram of the static-rapid GNSS field campaigns (in blue, Table 2), and the satellite data used in this study as master image (in red) or slave image (in green, see Table 3 for more details). Gray shaded areas represent eruptive periods.

22 days. During this short period, only a few radar images were acquired that could be used as slave images for interferograms covering the July eruption and/or as master image for interferograms covering the August eruption. Nevertheless, the amount and diversity of radar data available for each eruption make it possible to retrieve the 3-D displacement components with an unprecedented accuracy, as discussed later in the paper.

2.1.2. Interferograms and 3-D displacement computations

2.1.2.1. Interferogram computation. Our interferograms were produced with the DIAPASON© software (CNES/Altamira-Information, 1996) using the two-pass method described by Massonnet and Feigl (1998). The contribution of the orbital trajectories to the interferograms was modeled and removed using the precise orbit state vectors provided by Space Agencies. A 5 m Lidar DEM, produced by the French Geographic Institute (IGN) in 2008–2009, has been used to model and remove the topographic contribution. The IGN Lidar DEM was also used to provide a common geographic frame (UTM-WGS84) for the interferometric products so that all interferograms have exactly the same spatial coverage.

2.1.2.2. 3-D displacement computation. Full 3-D displacement vectors can be retrieved by inverting at least three independent interferograms spanning the same event and produced from data acquired under different acquisition geometries (Wright et al., 2004). The east-west (EW) component can be resolved with a high degree of accuracy by combining interferograms produced from data acquired during both ascending and descending passes. The Up-Down (UD) component can be obtained by combining both low incidence angle and high incidence angle

interferograms. The accuracy of the UD component, however, is always lower than that of the EW component; the ground surface being only viewable from above. The low heading angles of past and current radar satellites make the north-south (NS) component difficult to determine with reasonable accuracy. Wright et al. (2004) mentioned the possibility of resolving the NS component by combining InSAR data produced from image couples acquired both by right-looking and left-looking radars. This possibility has been made possible in the late 2000s, when the Cosmo-Skymed, RADARSAT-2 and ALOS-2 satellites started to acquire some left-looking radar images.

The prerequisite steps to determinate the 3-D displacement components are unwrapping, de-trending and interferograms scaling. Unwrapping of the interferograms (i.e. conversion from ambiguous to absolute phase) was carried out using the Snaphu algorithm (Chen and Zebker, 2002). Most of the X-band and C-band interferograms show good coherence for the arid Enclos Fouqué caldera but are poorly coherent on the vegetated external flanks of the volcano (see examples on Fig. 3 and Appendix A). As a consequence, the unwrapping algorithm generally fails to properly unwrap these external flanks; they were thus masked for all the subsequent steps of data processing. High spatial displacement rates near the eruptive fissures (in the range of ~ 1 to $10 \text{ mm} \cdot \text{m}^{-1}$) can also result in unwrapping errors on most of the X-band and C-band interferograms. Due to their low resolution in the azimuth ($\sim 14 \text{ m}$), the two Interferometric Wide Swath (IW) Sentinel-1 interferograms, spanning the February eruption, are significantly less coherent than the other interferograms (Appendix A), we therefore decided not to use them for the 3-D displacement component inversion. By contrast, the ALOS-2 interferograms show an excellent coherence everywhere, even on the vegetated external flanks of the volcano and the areas of high displacement rates (see examples on Fig. 3 and Appendix

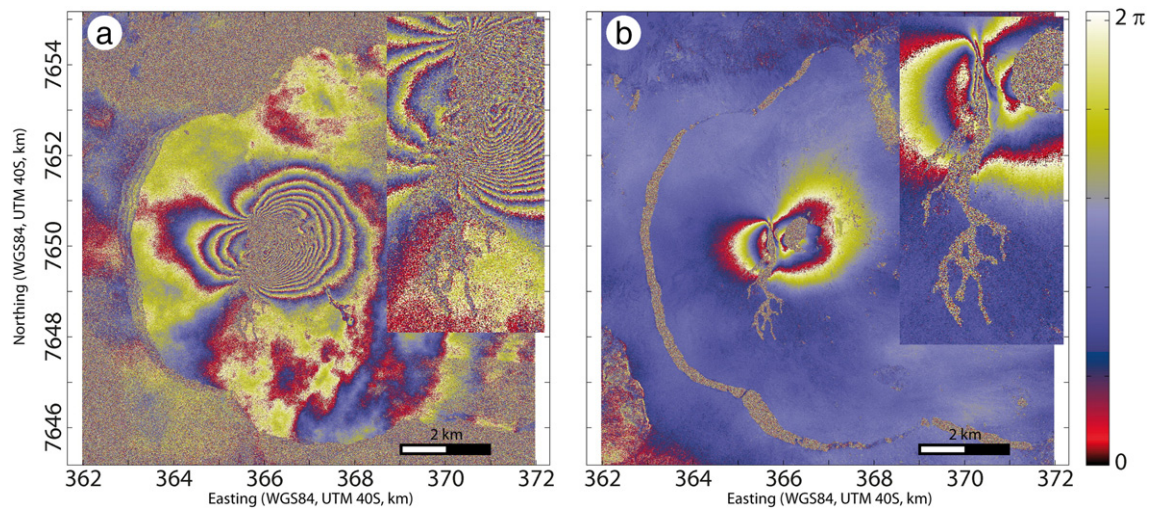


Fig. 3. Example of interferograms imaging displacement related to the February 2015 eruption. (a) TSX (X-band) descending interferogram spanning October 6, 2014 – March 9, 2015. Note the low coherence outside the Enclos Fouqué caldera as well as for the displacement near-field and for the February lava flows (enlarged view at the top right). (b) ALOS-2 Spotlight (L-band) ascending interferogram spanning January 23, 2015 – February 6, 2015. The displacement near field is clearly visible on the enlarged view whereas the February lava flows and the western part of the Dolomieu crater are not coherent. A complete phase cycle (red–blue–yellow) represents an increase in the Earth–satellite distance of 1.5 cm in (a) and 11.8 cm in (b). Coordinates in kilometers (WGS84, UTM 40S).

A), and can provide (in particular the ALOS-2 Spotlight interferograms) an exceptional view of the near-field displacement.

The objective of the de-trending step is to reduce the possible contributions of unwanted large wavelength interferometric signals, such as atmospheric artifacts or residual orbital ramps in order to reference the interferograms to a common zero phase origin. We de-trended each interferogram by removing a three-degree regression polynomial surface across the whole region of interest after masking the area affected by co-eruptive displacements and the low coherence areas. This surface is assumed to account for the large wavelength phase variation as a function of easting and northing. Removing or, at least, characterizing as accurately as possible atmospheric artifacts in interferograms still remains challenging on InSAR data analysis. Most of the approaches (Zebker et al., 1997; Beauducel et al., 2000; Hanssen, 2001; Remy et al., 2003, 2015; Li et al., 2006; Pavez et al., 2006; Puysségur et al., 2007; Doin et al., 2009; Fournier et al., 2011; Pinel et al., 2011, 2014) cannot be considered as universal solution, as they rely on specific geographic conditions or external data availability. At Piton de la Fournaise, the main difficulty comes from the strongly turbulent character of the atmosphere that makes inefficient the approaches based on the phase-elevation relation. In absence of a better usable approach, we assumed that both the interferograms de-trending and the use of a large amount of independent interferograms for the 3-D displacement components inversion contribute to the reduction of the atmospheric artifacts. A particular care was taken to accurately assess final displacements uncertainty assuming that it reflects, among other factors, the uncorrected atmospheric artifacts.

The final scaling step converts phases to LOS displacement by multiplying by $\lambda/(4\pi)$, where λ is the wavelength of the radar wave (i.e. $\lambda_{CSK} = 3.12$ cm, $\lambda_{TSX} = 3.10$ cm, $\lambda_{RS2} = 5.55$ cm, $\lambda_{S1} = 5.55$ cm, $\lambda_{ALOS2} = 23.84$ cm).

We then inverted maps of displacement components (EW, NS, and vertical) for each eruption from the independent co-eruptive interferograms using the following formulation (Wright et al., 2004):

$$\hat{u} = -[P^T \times V^{-1} \times P]^{-1} \times P^T \times V^{-1} \times R \quad (1)$$

where \hat{u} is the column vector containing the EW, NS and vertical components of displacement, P is the matrix containing the LOS unit vector for the independent co-eruptive interferograms, R is the column vector containing the LOS displacements measured from the independent co-eruptive interferograms and V is the $m \times m$ full variance-covariance matrix of the unwrapped, de-trended and scaled interferograms, where m is the total number of independent interferograms for a particular eruption. The estimated variances range between 1.4×10^{-5} m² and 2.4×10^{-3} m² with a mean value of 2.3×10^{-4} m² (Table 1) and the covariances range between 7.8×10^{-6} m² and 2.9×10^{-5} m². V is calculated on the same areas as for the polynomial surface calculation at the de-trending step. It is used to weight the inversion. It also allows producing an associated standard error map for each displacement map, as estimated from the square root of the diagonal elements of the posterior covariance matrix (Appendix B; Strang, 1986).

For each map, the displacement components were inverted on a pixel-by-pixel basis, after eliminating, for each interferogram, pixels whose coherence was below a fixed threshold and, for each whole interferometric dataset, pixels whose coherence standard deviation was above a fixed threshold. This coherence standard deviation is also calculated on a pixel-by-pixel basis for each interferogram dataset. The thresholds are fixed empirically (with coherence threshold = 0.33 and coherence standard deviation threshold in the range of 0.25 to 0.35). As a result, the number of independent LOS displacement data retained for the 3-D component inversion can differ between adjacent pixels. In order to limit this difference, all pixels with less than $m-2$ data available for inversion after thresholding were eliminated (i.e. $m = 9$ for the February eruption, $m = 10$ for the May eruption, $m = 8$

for the July and $m = 7$ for the August eruption; Table 1; Fig. 2; Appendix C). Finally, the missing areas, whose sizes do not exceed 2 pixels, were interpolated by computing the median of nearest neighbors in a 5×5 pixel window.

2.2. GNSS

The GNSS (Global Navigation Satellite System) receiver network is now the most developed deformation field network on Piton de la Fournaise with 24 permanent stations, as 1) modern receivers can record data from multiple types of GNSS satellites, which increases the overall accuracy of the calculated positions, and 2) accurate post-processing increases the reliability of the method.

The OVPF receivers comprise 15 Topcon GB1000, 3 Trimble NetRS, and 6 Trimble NetR9; 10 are installed on the terminal cone, 6 on the eastern flank, and 8 outside the Enclos Fouqué caldera (for this study we used only the ones located inside the coherent zones covered by InSAR, see Fig. 1). Each receiver has a sampling rate of 30 s, and the NetR9 receivers have a second session with a sampling rate of 1 s. Data are automatically transmitted to the OVPF by WI-FI and post-processed with the GAMIT/GLOBK software package (Herring et al., 2010) to give daily mm-precision solutions. For these calculations, GAMIT uses i) the precise ephemerides of the international GNSS Service (IGS); ii) a stable support network of 20 IGS stations off La Réunion Island scattered around the Indian Ocean islands and coasts; iii) a tested parameterization of the troposphere; and iv) models of ocean loading, Earth and lunar tides. Data are corrected from plate motion, deduced from the REUN IGS station located 15 km to the west of the summit and assumed not to be affected by any volcano deformation.

To complete and increase the density of GNSS measurements during eruptions, a network of stainless steel benchmarks (75 in 2015) has been established on the terminal cone. These benchmarks are measured during GNSS static-rapid field campaigns after each magma intrusion (Fig. 2; Table 2). The receivers used during the 2015 surveys were the multi-frequency, multi-constellation ProMark 800 GNSS Surveying System from Ashtech. Due to the large number of benchmarks the acquisition time at each point is now limited to 3 min with a rate of 1 measurement per second. These data are post-processed with the Spectra Precision Survey Office software and referenced to the permanent GITG station located just outside of the north-western part of the Enclos Fouqué caldera (~4 km from the summit; Fig. 1). Data precision measured by this rapid-static mode is about 2.5 cm horizontally and 4 cm vertically (versus a few mm horizontally and 1–2 cm vertically on the permanent recordings), which is good enough to study the large deformation linked to dike injections.

3. Results

Deformation at Piton de la Fournaise occurred on two time scales, with long-term low rates (the days or weeks preceding an eruption), and short-term high rates (the minutes or hours preceding an eruption; e.g. Peltier et al., 2009). In 2015, a low and nearly continuous long-term

Table 2

Dates (yyyy/mm/dd) of the static-rapid GNSS field campaigns, whose data are used in this study.

	Date (yyyy/mm/dd)
GNSS survey	2014/06/24 and 06/25
Start of the eruption	2015/02/04
GNSS survey	2015/02/09 and 02/16
Start of the eruption	2015/05/17
GNSS survey	2015/05/27
Start of the eruption	2015/07/31
GNSS survey	2015/08/10 and 08/11
Start of the eruption	2015/08/24
GNSS survey	2015/08/28 and 09/01

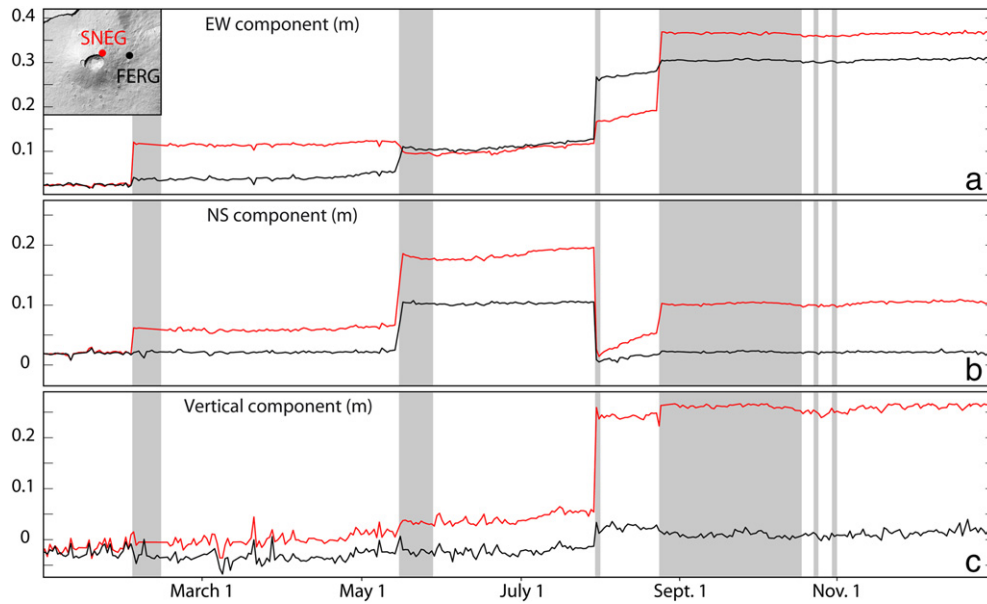


Fig. 4. Time series plots showing (a) east-west, (b) north-south, (c) and vertical displacements recorded on the SNEG (in red) and FERG (in black) permanent GNSS stations (see the inset for location) in 2015. Data are corrected for the plate motion. Gray shaded areas represent eruptive periods.

edifice inflation was recorded between each eruption by continuous GNSS data (Fig. 4), and was inferred to be a sign of deep fluid transfer that began in June 2014 (Peltier et al., 2016). Because of its low rate (0.03–0.1 mm/day before February 2015 and up to 0.5–2.5 mm/day in August 2015), this inter-eruptive edifice inflation was not well evidenced by InSAR. By contrast, the rapid strong deformation preceding the eruption by a few minutes/hours is well captured by InSAR. We thus focus below on the deformation linked to the eruptive periods.

3.1. Deformation pattern linked to the four 2015 eruptions

3-D displacements computed from interferograms provide east-west, north-south and vertical displacement maps associated with the four eruptions (Figs. 5, 6, 7, 8). For comparison, GNSS displacements covering the same eruptions are plotted together as colored filled circles. Note that for the February eruption, we did not take into consideration the data in the near-field of the low coherence areas located close

to the lava flows and eruptive vents (high standard error values in InSAR, see Section 3.3 for more details).

Overall, for each eruption, the amplitude of the associated horizontal and vertical displacements is decimetric and mostly distributed around the eruptive fissures, and extending from the summit zone. Displacements are well confined around the dike paths and do not extend very far beyond their extremities. Instead, the deformation spreads laterally to the dikes over a larger area (Figs. 5, 6, 7, 8), especially to the east. This leads to a typical and systematic pattern of lateral dike-associated ground deformation at Piton de la Fournaise: i.e. a clear asymmetry of the displacements on either side of the dikes, with a preferential eastward-seaward motion (e.g. Toutain et al., 1992; Sigmundsson et al., 1999; Froger et al., 2004; Fukushima et al., 2005, 2010; Peltier et al., 2007, 2008, 2009).

The February and August eruptions present roughly similar displacement patterns, typical of displacement induced by intrusion of a ~NS dike within the terminal cone, i.e. an asymmetric pattern with respect

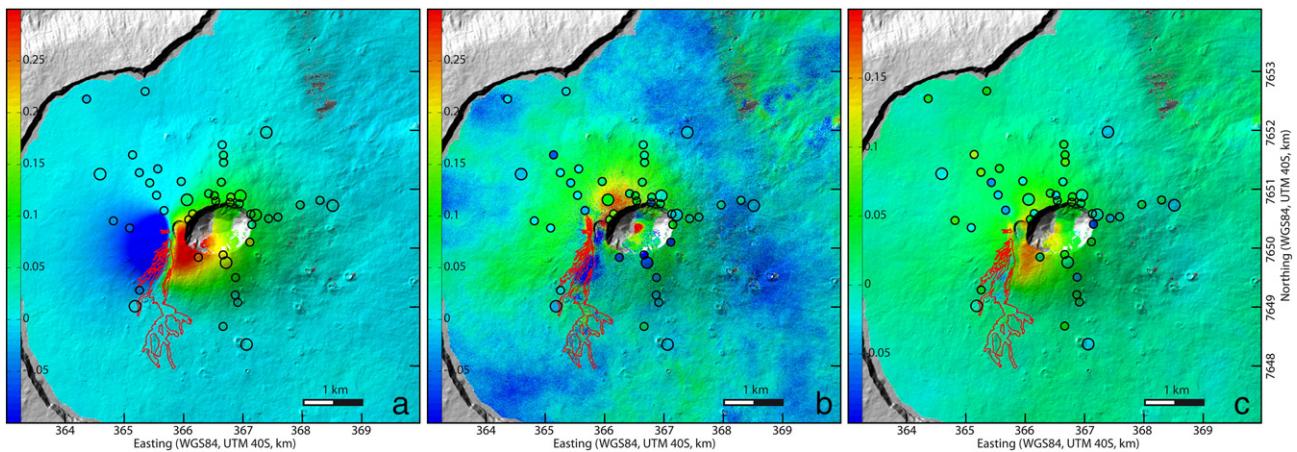


Fig. 5. Map of (a) east-west (b) north-south and (c) vertical displacements (in m) computed with InSAR data, covering the February 4, 2015 dike injection. The filled circles represent (a) east-west (b) north-south and (c) vertical displacements, covering the same dike injection, recorded at the permanent GNSS stations (large filled circles) and during the static-rapid GNSS field surveys (small filled circles). See Tables 1 and 2 for the precise dates of the satellite acquisitions and static-rapid GNSS field campaigns, respectively. For the permanent GNSS, the displacements have been calculated for the mean period covered by the interferograms. The lava field emplaced during this eruption is outlined in red. Low-coherence areas outside the Enclos Fouqué caldera are masked. Coordinates in kilometers (WGS84, UTM 40S).

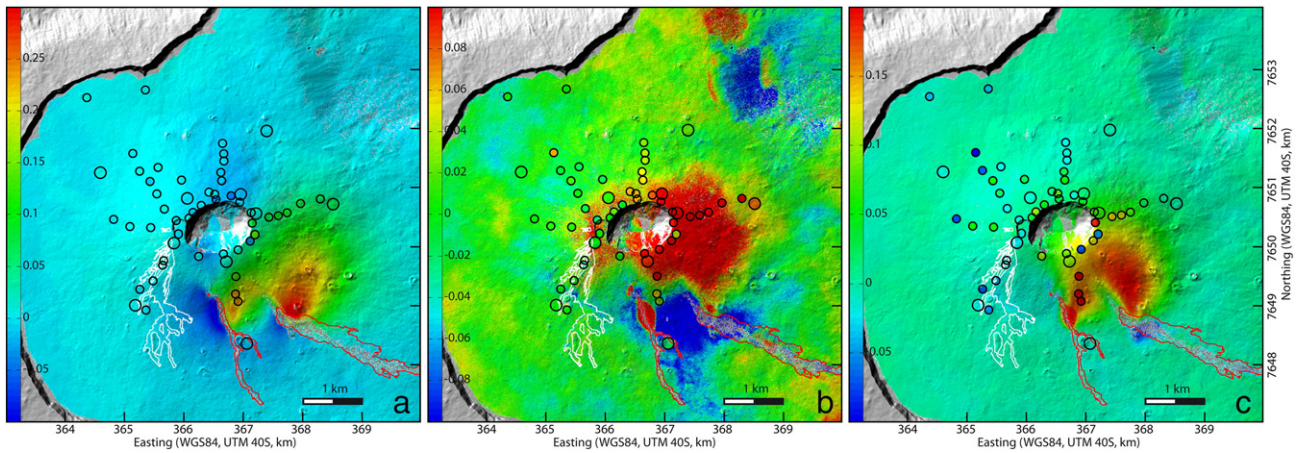


Fig. 6. Map of (a) east-west (b) north-south and (c) vertical displacements (in m) computed with InSAR data, covering the May 17, 2015 dike injection. The filled circles represent (a) east-west (b) north-south and (c) vertical displacements, covering the same dike injection, recorded at the permanent GNSS stations (large filled circles) and during the static-rapid GNSS field surveys (small filled circles). See Tables 1 and 2 for the precise dates of the satellite acquisitions and static-rapid GNSS field campaigns, respectively. For the permanent GNSS, the displacements have been calculated for the mean period covered by the interferograms. The lava field emplaced during this eruption is outlined in red, and the previous 2015 one is outlined in white. Low-coherence areas outside the Encls Fouqué caldera are masked. Coordinates in kilometers (WGS84, UTM 40S).

to the ~NS eruptive fissures, with strong eastward and upward displacements to the east of the eruptive fissure and low westward and vertical displacements to the west. The May and July eruptions are more distal, and regarding their displacement patterns they involve dikes oriented ~N140°E and ~N30°E, respectively. However, the associated displacements show the same general characteristics that were observed in February and August: a clear asymmetric pattern with strong eastward and upward displacement to the east of the fissures. In the case of the May eruption, this general scheme is duplicated due to the activity of two parallel eruptive fissures (signs of two en-echelon dike terminations or the intrusion of two parallel dikes); the displacements associated with the eastern fissure are significantly stronger and wider than those of the western one, an observation consistent with the difference of lava volume emitted by each fissure (Fig. 6).

For all events, amplitudes of horizontal displacements are greater than vertical ones, and the EW displacements are greater than the NS ones. The 3-D ground displacements do not exceed 65 cm, the maximum (64 cm) being recorded in July 2015, ~800 m east of the eruptive fissure (Fig. 7).

3.2. Consistency between the GNSS and InSAR methods

To evaluate the consistency between the GNSS and InSAR datasets, we retrieved the 3-D displacements derived from InSAR at the exact location of each GNSS stations or benchmarks by interpolating InSAR data with a Kriging regression.

We plotted the GNSS-InSAR residual values of the EW, NS and vertical displacements associated with the four 2015 eruptions on Fig. 9. The best results are found for the EW component, where, depending of the event, 79 to 100% of the data have GNSS-InSAR residual values <2.5 cm, and 96 to 100% of the data have GNSS-InSAR residual values <5 cm (Fig. 9; Table 3). By contrast, the largest discrepancies for all events are observed on the NS component, with 6% to 51% (depending of the events) of the data showing GNSS-InSAR residual values <2.5 cm (Fig. 9; Table 3). The worst results of the comparison are observed for the NS component of the August 2015 dike injection, with a mean discrepancy of 6.4 and 9.7 cm between displacements deduced from InSAR and permanent and re-iterated GNSS data (i.e. static-rapid GNSS surveys), respectively. For the vertical component, the mean

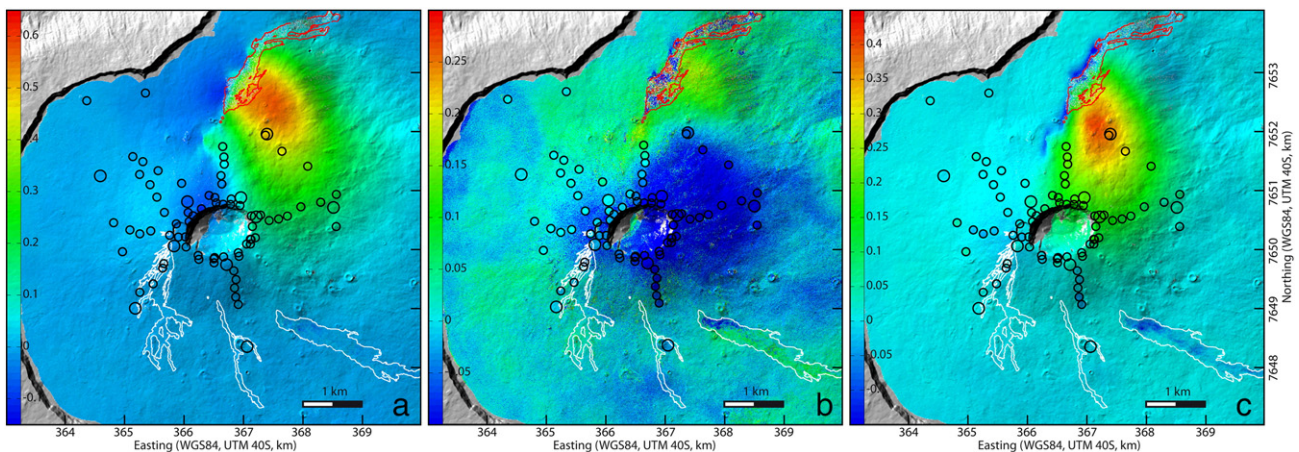


Fig. 7. Map of (a) east-west (b) north-south and (c) vertical displacements (in m) computed with InSAR data, covering the July 31, 2015 dike injection. The filled circles represent (a) east-west (b) north-south and (c) vertical displacements, covering the same dike injection, recorded at the permanent GNSS stations (large filled circles) and during the static-rapid GNSS field surveys (small filled circles). See Tables 1 and 2 for the precise dates of the satellite acquisitions and static-rapid GNSS field campaigns, respectively. For the permanent GNSS, the displacements have been calculated for the mean period covered by the interferograms. The lava field emplaced during this eruption is outlined in red, and the previous 2015 ones are outlined in white. Low-coherence areas outside the Encls Fouqué caldera are masked. Coordinates in kilometers (WGS84, UTM 40S).

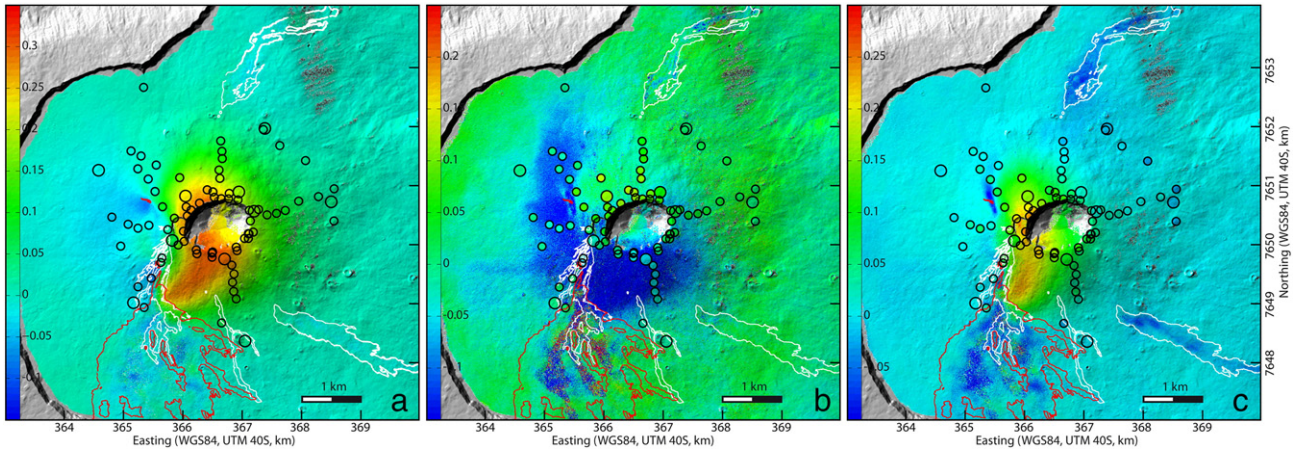


Fig. 8. Map of (a) east-west (b) north-south and (c) vertical displacements (in m) computed with InSAR data, covering the August 24, 2015 dike injection. The filled circles represent (a) east-west (b) north-south and (c) vertical displacements, covering the same dike injection, recorded at the permanent GNSS stations (large filled circles) and during the static-rapid GNSS field surveys). See Tables 1 and 2 for the precise dates of the satellite acquisitions and static-rapid GNSS field campaigns, respectively. For the permanent GNSS, the displacements have been calculated for the mean period covered by the interferograms. The lava field emplaced during this eruption is outlined in red, and the previous 2015 ones are outlined in white. Low-coherence areas outside the Enclos Fouqué caldera are masked. Coordinates in kilometers (WGS84, UTM 40S).

discrepancies between the two methods ranged between 1.7 and 4.3 cm for the February and May 2015 events, and between 0.9 and 2.1 cm for the July and August 2015 events. As for the two other components, the comparison results for the vertical component are better with the permanent GNSS data than with the rapid-static GNSS data, with a mean discrepancy of 0.9–2.9 cm and 2.1–4.3 cm, respectively.

Furthermore, a systematic shift between the InSAR data and the permanent GNSS data for February, May and August is observed, i.e. a westward (InSAR < GNSS EW displacements) and upward shift (InSAR > GNSS NS displacements; Fig. 9). This is not as clear on the static-rapid GNSS data. For August, a clear southward shift between the InSAR data and the static-rapid GNSS data is also observed (InSAR < GNSS vertical displacements).

For the points located on the terminal cone, the GNSS-InSAR residual values seem to correlate with elevation (Fig. D1 in Appendix D).

Such discrepancies between the two datasets could be attributed to the errors associated with each method.

Contrary to GNSS, there is no standard procedure for InSAR uncertainty mitigation since the uncertainties have various origins and are specific to each case. We present below, in more detail, the derived-InSAR displacement uncertainty obtained for our 3D displacement calculation.

3.3. Derived-InSAR displacement uncertainty

3.3.1. InSAR displacement standard error maps

The InSAR displacement standard error maps, obtained as output of the 3-D component inversion procedure (Appendix B), provide an estimation of the displacement uncertainty derived from InSAR. They reflect all the inconsistencies between the interferograms used for each eruption, weighted by the data variance-covariance matrix. The EW displacement standard error maps are shown, for each eruption, in Fig. 10. The NS and UD standard error maps are linearly proportional to the EW ones and will not be described further here. The largest standard errors occur in areas covered by recent lava flows. For instance, the lava field emplaced in May 2015 is especially well visible on the July 2015 EW displacement standard error map (Fig. 10c), and even remains visible on the August 2015 one (Fig. 10d). For the February and May 2005 displacement standard error maps, areas of strong standard error affect the upper part of their corresponding lava flows (Fig. 10a, b).

For all four eruptions, the displacement standard error is always larger on the Piton de la Fournaise terminal cone, suggesting some correlation with elevation (Fig. D2 in Appendix D). A clear correlation also

exists between displacement standard error and the slope (Fig. D3 in Appendix D).

For each eruption, we have analyzed the standard error in more detail, considering both the entire Enclos Fouqué area and the area affected by co-eruptive displacements (i.e. the area inside the white contours in Fig. 10). The mean standard error calculated for the EW, NS and UD components on the entire Enclos Fouqué area ranges between 4.7 and 6.2 mm, 28.7 and 40.7 mm, and 5.9 and 9.5 mm, respectively (Table 4), whereas the mean standard error calculated on the areas affected by co-eruptive displacements is slightly higher ($6.5 \text{ mm} < \sigma_{EW} < 8.5 \text{ mm}$, $32.8 < \sigma_{NS} < 65 \text{ mm}$, and $7.4 \text{ mm} < \sigma_{UD} < 15 \text{ mm}$, respectively); a result we attribute mainly to the fact that these areas include the terminal cone. These standard errors can be regarded as estimators of the InSAR 3-D displacement precision. However, in the case where interferograms used for a particular eruption are biased in exactly the same way by certain artifacts (e.g. some atmospheric components), the corresponding standard error will be null. So, to obtain a view as complete as possible of the InSAR displacement uncertainties we also carried out a statistical analysis of the 3-D displacement components far-field, where the co-eruptive displacements are supposed to be null (i.e. the areas outside the white contours in Fig. 10). Thus, we obtained both an estimator of the InSAR displacement accuracy and a second estimator of the displacement precision (i.e. the mean and the standard deviation of the displacement far field, Table 4). The two precision estimations are generally very close (mean difference of ~3 mm). The accuracy estimate is very good with a mean displacement for the area supposedly unaffected by co-eruptive displacement ranging between 0 mm and 0.8 mm, apart from the NS displacements of the July 2015 eruption, which present a systematic bias of about 5.6 mm.

3.3.2. Geometric dilution of precision

In order to quantify the influence of the InSAR dataset geometry on the precision of the inverted 3-D displacement components, we also calculated, for each eruption, the geometric dilution of precision (GDOP) for different configurations of the dataset using the following formulation (Strang and Borre, 1997; Wright et al., 2004; Table 4; Table E1 in Appendix E):

$$\sum_u = \sigma^2 [P^T P]^{-1} \quad (2)$$

where the GDOP values for the EW, NS and UD components are given by the square root of the diagonal terms of \sum_u when σ is set to 1. σ is the

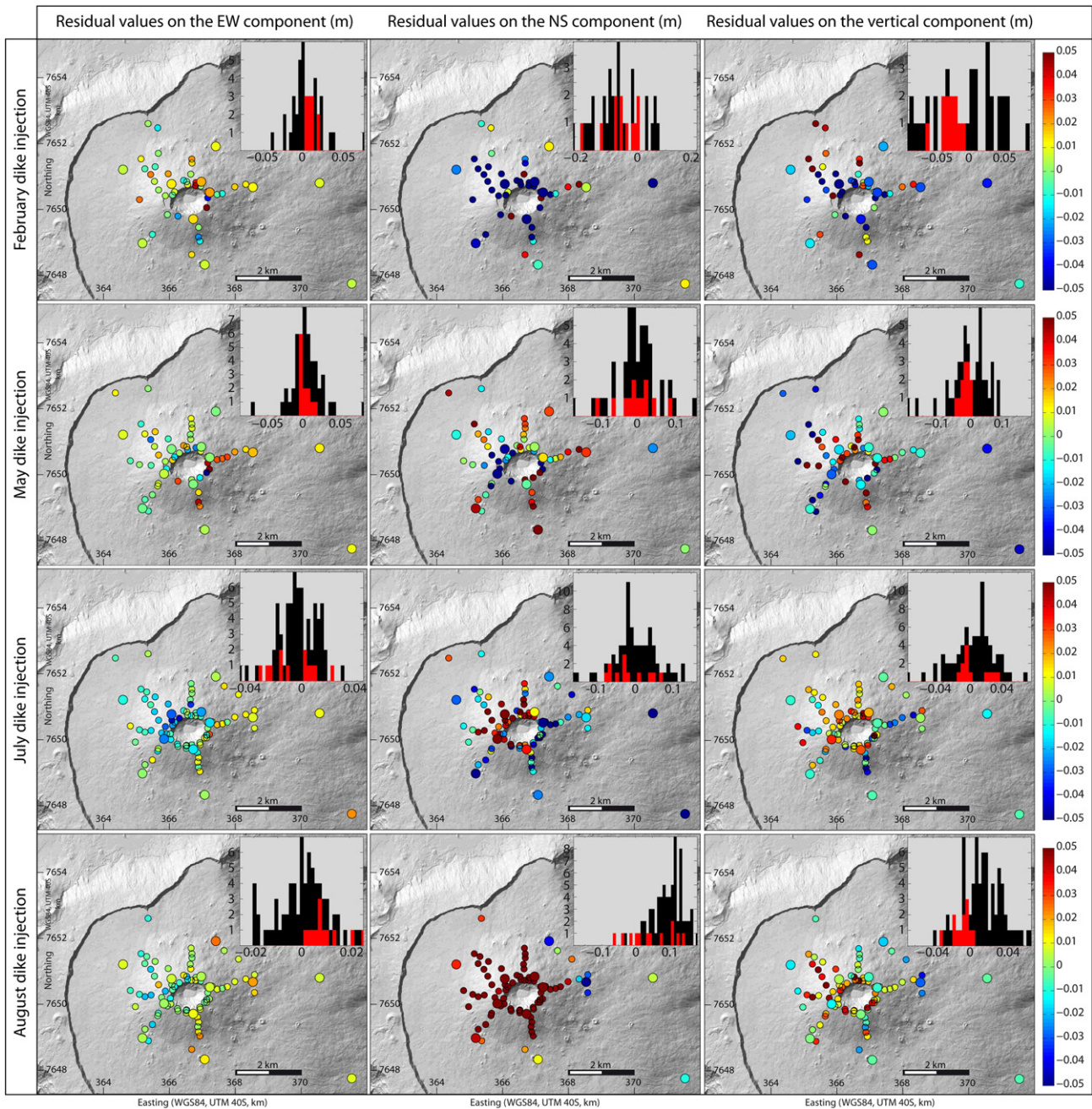


Fig. 9. GNSS-InSAR residual values (in m) of the east-west, north-south and vertical displacements associated with the four 2015 eruptions, and the associated histogram distribution (in red: permanent GNSS data, in black: static-rapid GNSS data). For a better comparison, the scale of the color bar is the same for each inset, leading to some color saturation, especially for the NS component. Coordinates in kilometers (WGS84, UTM 40S).

standard deviation of errors in the independent co-eruptive interferograms. P is the matrix containing the LOS unit vector for the independent co-eruptive interferograms.

Not surprisingly, the precision of the inverted 3-D displacement components correlates approximately with the GDOP values (i.e. the lowest the GDOP, the highest the precision of the inverted 3-D displacement components). The three last eruptions of 2015 have significantly lower GDOP than that of the February eruption (Table C1 in Appendix E). These differences in GDOP are linked to the presence of ALOS-2 data, acquired with left-looking radar antenna, in the three datasets used for the inversion of the May, July and August 3-D displacement components, while all the data used for February were only acquired with right-looking radar antennas.

4. Discussion

4.1. Ground displacement pattern associated with the 2015 eruptions at Piton de la Fournaise

The ground deformation pattern associated with the dike emplacements feeding the four eruptions of 2015 at Piton de la Fournaise are typical of this volcano. Dikes always initiate from the shallow magma feeding system located below the summit of the volcano (e.g. Peltier et al., 2009), and the associated ground displacements thus always radiate from the summit borders (Figs. 5, 6, 7, 8). During their opening and migration, dikes can be caught by one of the rift zones (Fig. 1) and can propagate laterally, generating flank displacements, as observed during the four eruptions of 2015; over a very short distance in February (to the

Table 3

Discrepancy between GNSS and InSAR data. For each eruption and each component (east-west: E, north-south: N, vertical: U) the percentage of data with a residual <2.5 cm and 5 cm between GNSS and InSAR methods is reported. The mean discrepancy (in cm) between the two methods is also reported.

	Res < 2.5 cm E comp. (in %)	Res < 2.5 cm N comp. (in %)	Res < 2.5 cm U comp. (in %)	Res < 5 cm E comp. (in %)	Res < 5 cm N comp. (in %)	Res < 5 cm U comp. (in %)	Mean discrepancy E N U (in cm)
February 2015							
GNSS survey	86	19	27	97	32	59	1.5 7.1 4.2
Permanent GNSS	100	36	36	100	64	91	1.1 5.2 2.9
May 2015							
GNSS survey	79	51	34	96	72	70	1.7 3.8 4.3
Permanent GNSS	100	50	75	100	83	100	0.5 3.2 1.7
July 2015							
GNSS survey	93	44	69	100	73	96	1.1 4.2 2.1
Permanent GNSS	83	25	83	100	58	100	1.4 4.4 1.3
August 2015							
GNSS survey	100	6	66	100	17	93	0.8 9.7 2.1
Permanent GNSS	92	25	92	100	50	100	1.0 6.4 0.9

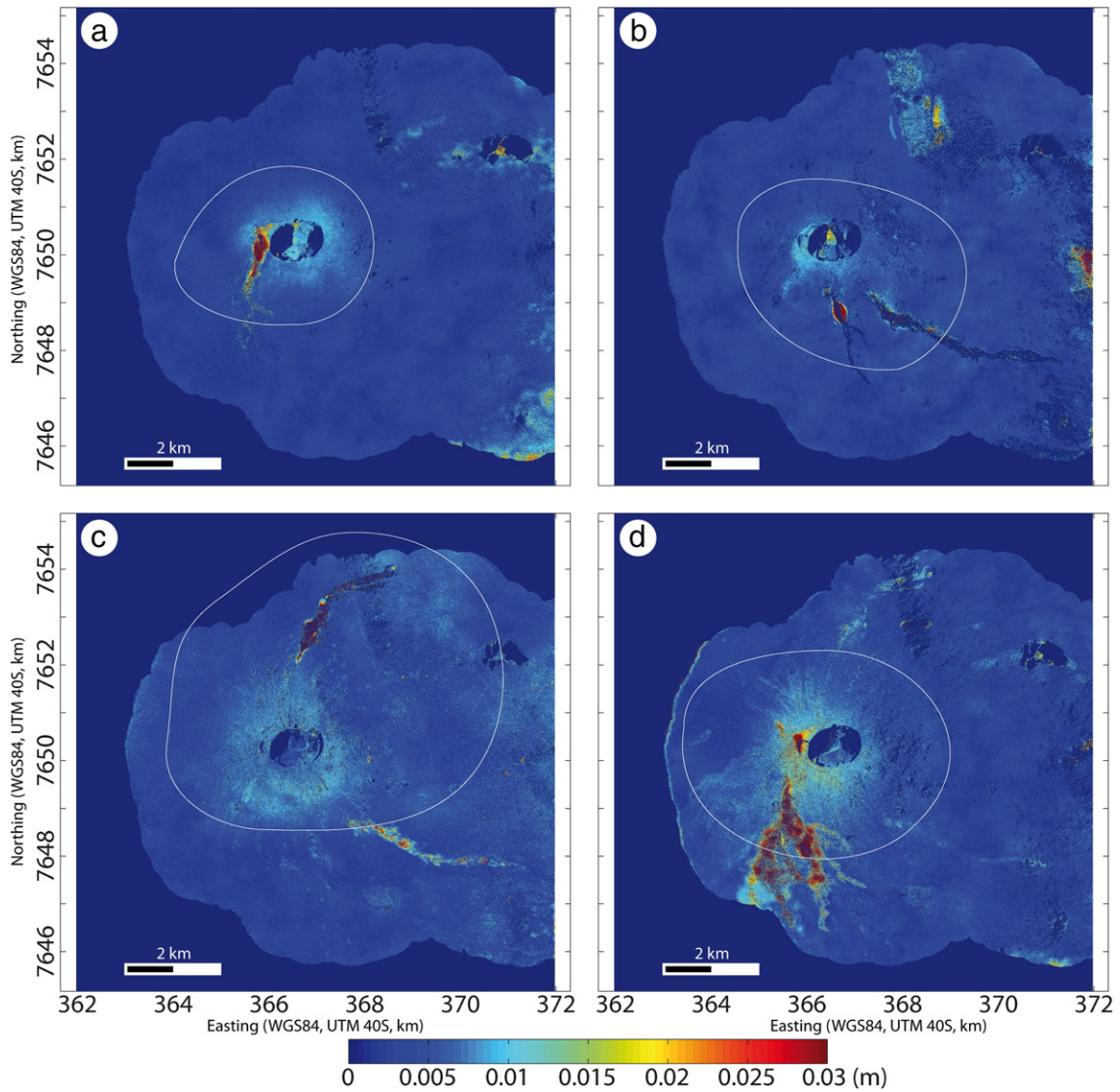


Fig. 10. Displacement standard error maps, for the EW component, as estimated from the square root of the diagonal elements of the posterior covariance matrix (Appendix B, Strang, 1986). (a) February 2015 eruption; (b) May 2015 eruption; (c) July 2015 eruption; (d) August 2015 eruption. White contour delineates outer and inner zones considered for calculation of mean standard errors and mean displacement reported in Table 4. Dark blue corresponds to low-coherence masked areas. Coordinates in kilometers (WGS84, UTM 40S).

Table 4
Mean standard errors and mean displacements in meters for each 2015 eruption and each component. All standard errors are given for 1 σ . ϵ_x , ϵ_y , ϵ_z are the geometric dilution of precision of the EW, NS and UD components estimated for $\sigma = 1$, σ being the standard error on the unwrapped, de-trended and scaled interferograms.

	February 2015	May 2015	July 2015	August 2015
Mean EW standard error, entire zone	0.0047 \pm 0.0032	0.0053 \pm 0.0034	0.0060 \pm 0.0038	0.0062 \pm 0.0058
Mean EW standard error, inner zone	0.0074 \pm 0.0053	0.0065 \pm 0.0050	0.0068 \pm 0.0042	0.0085 \pm 0.0080
Mean EW displacement and StD, outer zone	-0.0001 \pm 0.0045	0.0000 \pm 0.0058	-0.0003 \pm 0.0073	-0.0004 \pm 0.0068
ϵ_x	0.5	0.56	0.52	0.55
Mean NS standard error, entire zone	0.0407 \pm 0.0300	0.0304 \pm 0.0199	0.0287 \pm 0.0191	0.0306 \pm 0.0488
Mean NS standard error, inner zone	0.0650 \pm 0.0500	0.0378 \pm 0.0300	0.0328 \pm 0.0216	0.0433 \pm 0.0715
Mean NS displacement, and StD outer zone	-0.0001 \pm 0.0400	0.0006 \pm 0.0342	0.0056 \pm 0.0368	-0.0006 \pm 0.0445
ϵ_y	6.66	3.04	2.54	3.03
Mean UD standard error, entire zone	0.0095 \pm 0.0068	0.0059 \pm 0.0038	0.0069 \pm 0.0042	0.0090 \pm 0.0116
Mean UD standard error, inner zone	0.0150 \pm 0.0112	0.0074 \pm 0.0057	0.0079 \pm 0.0047	0.0126 \pm 0.0168
Mean UD displacement and StD, outer zone	0.0002 \pm 0.0094	0.0002 \pm 0.0063	0.0008 \pm 0.0088	-0.0004 \pm 0.0120
ϵ_z	1.59	0.61	0.62	0.65

S), and longer ones in May (to the SE), July (to the N) and August (to the S).

The asymmetric displacement pattern observed for the 2015 eruption is also recurrent at Piton de la Fournaise. Inversion modeling of GNSS or InSAR data linked to these eruptions or previous ones in a purely elastic medium reveals the involvement of dikes with a low dip to the east (e.g. Froger et al., 2004; Fukushima et al., 2005, 2010; Peltier et al., 2007, 2009; Samsonov et al., 2017). But this shape is not necessarily representative of the reality. Indeed, the eastern flank, opened toward the sea, is known to be unstable, and to undergo continuous sliding even during rest periods (e.g. Brenguier et al., 2012; Peltier et al., 2015; Staudacher and Peltier, 2016). Got et al. (2013) used elasto-plastic modeling to explain this pattern, due to the effect of the rock rheology and strength. During dike injections, stress accumulated up to the plastic threshold of the medium, leading to large eastern seaward flank motion. This strain weakening can also arise from shearing along a planar structure (e.g. Chaput et al., 2014). This pattern seems to have been present for a long time, at least for 1950–2015, a period during which a total of 9.2 ± 2.5 m eastward seaward displacement has been recorded to the east of the summit compared to a total of 1.3 ± 2.5 m to the west (Derrien et al., 2015).

In 2015, maximum ground displacements were observed during the July dike injection. This eruption was the most distant of the four 2015 events (~2600 m from the Dolomieu crater northern rim), and recorded the highest mean output rates at the surface (~7.7 m³/s versus 1.4–6 m³/s for the three other events; Peltier et al., 2016). This reveals that a higher overpressure was involved in the dike injection toward the surface, which was likely at the origin of the greater ground displacements at the surface.

4.2. Agreements and disagreements between the methods

The comparison we made between ground displacements derived from InSAR and GNSS field receivers are in overall good agreement (with most of the residuals <2.5 cm for the EW component and <5 cm for the vertical component, thus within the error bar of each method; Table 3), except for the NS component. The north-south component is the least sensitive to ground displacement for near-polar orbiting satellites. As described in the “Methods” section, the low heading angles of radar satellites make the NS component difficult to determine with a high degree of accuracy. This leads to large discrepancies on this component, generally of >5 cm (Fig. 9, Table 3) although the use of left-looking images has made it possible to improve significantly the NS component precision.

4.2.1. Influence of the distinct periods considered for each datasets

Various sources of errors can explain the discrepancy between GNSS and derived-InSAR data. The most obvious is the distinct periods

covered by each dataset (Fig. 2; Tables 1, 2). Combining interferograms covering different periods is already an intrinsic source of uncertainty in InSAR measurements. Inter-eruptive displacements in 2015 were low (often <2 cm of cumulated displacement in the month preceding an eruption; Peltier et al., 2016) compared to the co-intrusive ones, so most of the displacements mapped on Figs. 5, 6, 7, 8 were generated during the dike injection toward the surface, that preceded the eruption by a few minutes/hours. However, we used the permanent GNSS stations to test the influence of the different periods on the results by comparing InSAR-derived data with different periods of GNSS data (minimum extreme dates, maximum extreme dates, mean dates of the InSAR dataset used to process the displacement maps, Table 1). Our results confirm that the integration of a few days/weeks of inter-eruptive period does not affect the quality of our comparison (see Appendix F). Note that the GNSS-InSAR residual values are most often lower for the GNSS permanent data than for the GNSS survey data (Table 3). Our test shows that this is most probably linked to differences in precision rather than to the distinct periods covered by the two datasets; because of the short time acquisitions of the measurements during the static-rapid GNSS surveys (only 3 min compared to continuous acquisition for daily solutions from the permanent stations), the precision is lower (a few cm) than that for the GNSS permanent station measurements (a few mm).

Thus, having excluded the hypothesis on the distinct periods covered by the two datasets, the error sources must be attributed to the methods themselves. This concerns mainly uncorrected atmospheric effects in InSAR (see below) and larger errors on the vertical GNSS component (most of the GNSS-InSAR residuals are <5 cm on the vertical component, whereas most are <2.5 cm on the EW component; Table 3). Due to the limited perspective of the satellites from which the height is measured, the vertical component of GNSS data is often two to five times less accurate than the horizontal one. In the same way, the accuracy of the vertical component deduced from InSAR is always lower because the ground surface is only viewed from above.

4.2.2. Origins of InSAR displacement uncertainty

For a given eruption, the interferograms can cover different time periods resulting in at least two possible sources of inconsistency: (i) inter-eruptive displacement recorded over different time periods (even if inter-eruptive displacement was low during the considered periods, Fig. 4), and (ii) different uncorrected atmospheric artifacts. In addition, the interferograms can have different sensitivity to topography, depending on their perpendicular baseline (Massonnet and Feigl, 1998). This effect induces inconsistencies between interferograms in the same dataset and thus a strong standard error on the 3-D displacement components. As a result, any topographic error in the DEM will induce an inconsistency in the interferometric dataset. The correlation between InSAR displacement standard errors and the local slope

(Fig. D3 in Appendix D) could be explained by a possible mismatch in the georeferencing of some interferograms, inducing topographic residuals, which are particularly marked where the slopes are locally steep. Other inconsistencies can come from unwrapping errors or from poorly coherent areas that have not been properly masked.

The high standard errors observed in the near-field of the eruptive vents, lava flows or inside the Dolomieu crater are directly linked to unwrapping problems due to incoherence; either because of phase aliasing where the displacement gradient is too strong, or new lava flow emplacements, landslides or rockfalls inside the Dolomieu crater (Fig. 10). This explains the discrepancy observed close to the eruptive vents and lava flows in May 2015 (Figs. 6, 9). For the specific case of recent lava flows, the high standard errors result from both (i) contraction and subsidence of lava flows imaged at different stages by each interferogram and (ii) loss of coherence due to lava flow emplacement that, in some places, has not been properly masked.

The increase in standard error on the terminal cone correlated with the relief - especially above an altitude of 2100–2200 m (Fig. 10; Appendix D) - could be explained by the effect of possible residual atmospheric artifacts that have not been properly corrected for in some interferograms. Indeed, (i) the atmospheric component is often partially correlated with elevation for volcanic edifices (Beauducel et al., 2000; Remy et al., 2015), (ii) our de-trending procedure only allows the largest artifacts to be removed, and (iii) the terminal cone zone is always masked during the de-trending procedure. Another explanation would be the effect of a negative gradient of the interferometric coherence versus elevation on the terminal cone. We observed a coarse negative correlation between coherence and elevation between 2200 m and 2600 m (~elevation of the terminal cone) for the last three eruptions of 2015 (Appendix D). It is less marked for the February 2015 eruption. Such a negative correlation could be explained by changes in the geometric or dielectric properties of the scatterers on the ground surface that could be dependent on the elevation and/or the distance to the summit craters. For example, the changes in soil moisture can be influenced both by the precipitation regime and the proportion of cinder and scoriaeous material constituting the soil, two factors that can vary as a function of both elevation and distance from the summit.

Such residual atmospheric artifacts and negative gradients of the interferometric coherence versus elevation would be at the origin of the systematic shifts observed between the InSAR and the permanent GNSS data on the terminal cone (Fig. 9).

4.3. Possible improvements

The use of InSAR data with multiple acquisition geometries, and in particular left-looking data, allowed us to obtain precision on the NS component close to that of the rapid-static GNSS data (standard error of between 2 and 4 cm for the NS displacements calculated with the dataset including left-looking data, compared to between 4 and 6 cm without this additional data, Table 4). However, the precision on the NS InSAR component remains about 4 to 6 times lower than that on the EW and UD components, respectively. The pixel offset tracking method, by SAR amplitude image correlation, has been demonstrated to be efficacious in the determination of the NS component in the case of large displacements (Wright et al., 2006; Grandin et al., 2009). In our case, however, where the maximum NS displacements are about a few tens of cm, the theoretical accuracy of this technique - in the order of one tenth of the spatial resolution, i.e., here about half a meter - is clearly inadequate. The Multiple-Aperture Interferometry (MAI) provides an alternative approach for the characterization of the NS component. This method is based on the formation of one forward-looking and one backward-looking image from one SAR image by sub-aperture processing techniques (Bechor and Zebker, 2006; Jung et al., 2009). By calculating the phase difference between a forward-looking and a backward-looking interferogram, it is then possible to image the displacement in the along-track direction (i.e. a

direction much more sensitive to NS displacement than the across-track direction) with a theoretical accuracy about three times better than that of the pixel offset tracking method (Pinel et al., 2014). In our case, the MAI approach is a particularly attractive alternative due to the availability, for all the 2015 eruptions, of ALOS-2 spotlight data. In this acquisition mode, the antenna is steered, as the satellite moves, in order to illuminate the same target on the ground, so that the first half of the acquisition is made forward-looking and the second half backward-looking. With an azimuth resolution of about 1 m, one could theoretically expect a final accuracy on the NS displacement component in the order of a few cm.

Grandin et al. (2016) have recently demonstrated the possibility to retrieve the full 3-D displacement field associated with the 2015 $M_w 8.3$ Illapel earthquake (Chile) from IW Sentinel-1 data, combining both classical across-track interferometry and burst overlap interferometry. Burst overlap interferometry consists in determining the along-track component of ground displacement from the double-difference between backward- and forward-looking interferograms within regions of burst overlap in IW Sentinel-1 data. As overlap regions represent about 10% of the burst length, Grandin et al. (2016) had to interpolate between successive burst overlaps to obtain a continuous along-track displacement field. This approach only characterizes the largest wavelengths of the displacement field. In our case, since Piton de la Fournaise is entirely covered by only one to two Sentinel-1 bursts (depending the pass), burst overlap interferometry is clearly not adapted to measure co-ruptive displacement, which the spatial distribution typically ranges from few hundred of meters to some kilometers.

The ALOS-2 data could also be used more optimally than we have done here to determine the near-field displacement. In our current processing chain, we have used a unique coherence mask for all the interferograms in each dataset. This leads to loss of the near-field displacement, an area in which the ALOS-2 data provides exceptional information, but the X-band and C-band data are generally poorly coherent or at least difficult to unwrap properly. One solution could be to perform a more adaptive masking of the data and/or to use the information provided by ALOS-2 data to improve the unwrapping of X-band and C-band interferograms in the near-field.

Another way to improve determination of the 3-D displacement components is obviously by trying to reduce the atmospheric component in InSAR data, especially on the terminal cone. The usual approach, consisting of removing the correlated part of the atmospheric component using an empirical relation between phase and elevation (Remy et al., 2003; Lin et al., 2010; Shirzaei and Burgmann, 2012), is not useful here since there is no other relief on Piton de la Fournaise with the same elevation range as that of the terminal cone that could be used to adjust the empirical phase-elevation relation. An alternative solution is to exploit the data provided by the dense GNSS permanent network to perform 3-D tomography of the atmospheric phase delay (e.g. Wadge et al., 2002; Webley et al., 2002). Although this solution is an obvious way of making the best synergistic use of the GNSS and InSAR data at Piton de la Fournaise, it has not yet been implemented into a fully operational procedure. It appears as particularly promising to assess atmospheric artifact on the terminal cone, where the GNSS network is relatively dense with a mean distance of about 2 km between stations. In contrast, at the scale of the whole Piton de la Fournaise edifice, the mean distance between GNSS stations is ~7.3 km, so that one may expect to be able to correct by this way only the largest wavelengths of the atmospheric component.

Finally, the InSAR displacements can also be corrected for possible systematic bias by using the permanent GNSS data as a reference.

4.4. Complementarity of the InSAR and GNSS methods

In spite of its limitations discussed above and the future improvements needed, InSAR is a powerful tool to map ground deformation in volcanic areas, as has already been shown in many cases in the past at

Piton de la Fournaise, and elsewhere (e.g. Massonnet et al., 1993; Massonnet and Feigl, 1998; Jonsson et al., 1999; Dzurisin, 2000; Froger et al., 2001, 2004; Yun et al., 2006; Wauthier et al., 2009; Pinel et al., 2011, 2014; Brunori et al., 2012; Catry et al., 2015).

InSAR is especially well suited when ground displacement gradients are in the range of $\sim 1 \times 10^{-2}$ to $1 \text{ mm} \cdot \text{m}^{-1}$ and display a progressive pattern, as observed during dike injections in basaltic volcano areas.

InSAR offers clear advantages in the absence of a dense monitoring network, whether on the eccentric areas of field networks or on volcanoes not monitored by ground instruments. For instance, in May 2015 at Piton de la Fournaise most of the permanent stations and reiterated benchmarks were outside the deformation pattern, except the SE quarter of the terminal cone (Fig. 6). Such a pattern of huge deformation outside the field networks was already observed in April 2007, when an eastward motion of up to 1.4 m was detected by InSAR on the eastern flank, which was not equipped at that time with permanent GNSS receivers (Clarke et al., 2013; Froger et al., 2015).

The high spatial resolution of InSAR data is particularly useful to create a reliable numerical model of the displacement source. However, InSAR data generally provides a final view of the displacement that does not offer the possibility to assess how the source grew and propagated to the surface. By contrast, thanks to their high and continuous acquisition frequency, the permanent GNSS data provide clues as to the dynamics of magma transfer to the surface. So the two methods are very complementary. An efficient synergy between the two methods is to firstly use the InSAR data in order to fix, by a numerical modeling approach, the final geometry of the displacement source, and then incorporate the GNSS data to determine, for each time step, which part of this final geometry was subject to overpressure.

5. Conclusions

This paper is one of the first detailed studies to assess the reliability and consistency of the InSAR and GNSS techniques for measuring 3-D ground displacements on volcanoes during rapid changes. Our study confirms the consistency and the complementarity of the two methods to characterize (i) the ground deformation distribution at high spatial resolution (InSAR), and (ii) the dynamism (GNSS) associated with eruptive activity. Our evaluation carried out on the Piton de la Fournaise volcano allows us:

- to improve the precision of the InSAR-resulting 3-D data by the use of InSAR data with multiple acquisition geometries, and in particular left-looking data;
- to describe in detail the deformation pattern associated with the four 2015 eruptions, i.e. decimeter ground displacements asymmetrically distributed along the dike path, evidencing a preferential eastward motion;
- to quantify the discrepancies between InSAR and GNSS: apart from the NS component, InSAR and GNSS data are in overall agreement (most of the GNSS-InSAR residuals are $<2.5 \text{ cm}$ and $<5 \text{ cm}$ on the EW and vertical component, respectively, i.e. within the error bar of each method). Most of the discrepancies on the terminal cone would be attributed to uncorrected atmospheric effects.

Supplementary data to this article can be found online at <http://dx.doi.org/10.1016/j.jvolgeores.2017.03.027>.

Acknowledgments

This study was supported by INSU/CNRS (Institut National des Sciences de l'Univers, CNRS), through the National Service for Volcanological Observations, by ANR (Agence Nationale de la Recherche) through the GEOSUD-ANR-10-EQPX-20 project and by CNES (Centre National d'Etudes Spatiales) through the Kalideos project. We thank DLR and JAXA for providing the TerraSAR-X/TanDEM-X and the ALOS-2 data,

respectively, through the LAN #0237 project and the 4th ALOS RA #1287 project. We thank SEAS-OI (Survey of Environment Assisted by Satellite in the Indian Ocean) receiving station that provided RADARSAT-2 images for free (www.seas-oi.org). We thank the Sentinel-1 ESA team, especially P. Potin and Y.-L. Desnos for having made possible routine Sentinel-1 stripmap acquisitions on La Réunion. We are thankful to Philippe Durand (CNES) to have been a strong advocate of these stripmap acquisitions. All the interferograms were produced with the Diapason software except the two Sentinel-1A IW interferograms on February 2015 eruption that were calculated by Raphaël Grandin/IPGP with its own IW processing chain. Sentinel-1A stripmap interferograms for May 2015 eruption were calculated by Oscar Mora, Altamira-Information. The GNSS data used in this paper were collected by Observatoire Volcanologique du Piton de la Fournaise/Institut de Physique du Globe de Paris (OVPF/IPGP). We are grateful to two anonymous reviewers whose comments improved the manuscript. We would also like to especially thank Fran Van Wyk de Vries for early reviews of this manuscript. This is IPGP contribution number 3832 and Laboratory of Excellence ClerVolc contribution number 246.

References

- Aloisi, M., Mattia, M., Ferlito, C., Palano, M., Bruno, V., Cannavo, F., 2011. Imaging the multi-level magma reservoir at Mt. Etna volcano (Italy). *Geophys. Res. Lett.* 38, L16306. <http://dx.doi.org/10.1029/2011GL048488>.
- Bato, M.G., Froger, J.L., Harris, A.J.L., Villeneuve, N., 2016. Monitoring an effusive eruption at Piton de la Fournaise using radar and thermal infrared remote sensing data: insights into the October 2010 eruption and its lava flows. In: Harris, A.J.L., De Groeve, T., Garel, F., Carn, S.A. (Eds.), *Detecting, Modelling and Responding to Effusive Eruptions*. The Geological Society of London (Chapter: 30), <http://dx.doi.org/10.1144/SP426.30>.
- Beauducel, F., Briole, P., Froger, J.-L., 2000. Volcano-wide fringes in ERS synthetic aperture radar interferograms of Etna (1992–1998): deformation or tropospheric effect? *J. Geophys. Res.* 105 (B7), 16,391–16,402.
- Bechor, N.B.D., Zebker, H.A., 2006. Measuring two-dimensional movements using a single InSAR pair. *Geophys. Res. Lett.* 33. <http://dx.doi.org/10.1029/2006GL026883>.
- Biggs, J., Lu, Z., Fournier, T., Freymueller, J.T., 2010. Magma flux at Okmok Volcano, Alaska, from a joint inversion of continuous GPS, campaign GPS, and interferometric synthetic aperture radar. *J. Geophys. Res.* 115, B12401. <http://dx.doi.org/10.1029/2010JB007577>.
- Brenguier, F., Kowalski, P., Staudacher, T., Ferrazzini, V., Lauret, F., Boissier, P., Lemarchand, A., Pequegnat, C., Meric, O., Pardo, C., Peltier, A., Tait, S., Shapiro, N.M., Campillo, M., Di Muro, A., 2012. First results from the UnderVolc high resolution seismic and GPS network deployed on piton de la Fournaise volcano. *Seismol. Res. Lett.* 83 (7). <http://dx.doi.org/10.1785/gssrl.83.1.97>.
- Brunori, C.A., Bignami, C., Stramondo, S., Bustos, E., 2012. 20 years of active deformation on volcano caldera: joint analysis of InSAR and AInSAR techniques. *Int. J. Appl. Earth Obs. Geoinf.* 23:279–287. <http://dx.doi.org/10.1016/j.jag.2012.10.003>.
- Catry, T., Villeneuve, N., Froger, J.L., Maggio, G., 2015. InSAR monitoring using RADARSAT-2 data at Piton de la Fournaise (La Réunion) and Karthala (Grande Comore) volcanoes. *Geol. Soc. Lond., Spec. Publ.* 426 (SP426-20), <http://dx.doi.org/10.1144/SP426.20>.
- Chadwick Jr., W.W., Jónsson, S., Geist, D.J., Poland, M., Johnson, D.J., Batt, S., Harpp, K.S., Ruiz, A., 2011. The May 2005 eruption of Fernandina volcano, Galápagos: the first circumferential dike intrusion observed by GPS and InSAR. *Bull. Volcanol.* 73 (6): 679–697. <http://dx.doi.org/10.1007/s00445-010-0433-0>.
- Chaput, M., Pinel, V., Famin, V., Michon, L., Froger, J.-L., 2014. Cointrusive shear displacement by sill intrusion in a detachment: a numerical approach. *Geophys. Res. Lett.* 41:1937–1943. <http://dx.doi.org/10.1002/2013GL058813>.
- Chen, C.W., Zebker, H.A., 2002. Phase unwrapping for large SAR interferograms: statistical segmentation and generalized network models. *IEEE Trans. Geosci. Remote Sens.* 40 (8), 1709–1719.
- Clarke, D., Brenguier, F., Froger, J.-L., Shapiro, N.M., Peltier, A., Staudacher, T., 2013. Timing of a large volcanic flank movement at Piton de la Fournaise volcano using noise-based seismic monitoring and ground deformation measurements. *Geophys. J. Int.* 195 (2):1132–1140. <http://dx.doi.org/10.1093/gji/ggt276>.
- CNES, 1996. *Philosophy and Instructions for the Use of the DIAPASON Interferometry Software System Developed at CNES*.
- Derrien, A., Villeneuve, N., Peltier, A., Beauducel, B., 2015. Retrieving 65 years of volcano summit deformation from multitemporal structure from motion: the case of Piton de la Fournaise (La Réunion Island). *Geophys. Res. Lett.* 42. <http://dx.doi.org/10.1002/2015GL064820>.
- Doin, M.-P., Lasserre, C., Peltzer, G., Cavalié, O., Doubre, C., 2009. Corrections of stratified tropospheric delays in SAR interferometry: validation with global atmospheric models. *J. Appl. Geophys.* 69 (1), 35–50.
- Dzurisin, D., 2000. Volcano geodesy: challenges and opportunities for the 21st century. *Philos. Trans. R. Soc. Lond. A* 358, 1547–1566.
- Dzurisin, D., Wicks, C.W., Poland, M.P., 2012. History of surface displacements at the Yellowstone Caldera, Wyoming, from leveling surveys and InSAR observations: 1923–2008. *US Geol. Surv. Prof. Pap.* 1788, 68.

- Feigl, K.L., Le Mével, H., Tabrez Ali, S., Cordova, L., Andersen, N.L., DeMets, C., Singer, B.S., 2014. Rapid uplift in Laguna del Maule volcanic field of the Andean Southern Volcanic Zone (Chile) 2007–2012. *Geophys. J. Int.* 196 (2), 885–901.
- Fernández, J., Yub, T.-T., Rodríguez-Velasco, G., González-Matesanz, J., Romero, R., Rodríguez, G., Quirós, R., Dalda, A., Aparicio, A., Blanco, M.J., 2003. New geodetic monitoring system in the volcanic island of Tenerife, Canaries, Spain. Combination of InSAR and GPS techniques. *J. Volcanol. Geotherm. Res.* 124 (3–4), 241–253.
- Fournier, T.J., Pritchard, M.E., Finnegan, N., 2011. Accounting for atmospheric delays in InSAR data in a search for long-wavelength deformation in South America. *IEEE Trans. Geosci. Remote Sens.* 49 (10), 3856–3867.
- Froger, J.L., Merle, O., Briole, P., 2001. Active spreading and regional extension at Mount Etna imaged by SAR interferometry. *Earth Planet. Sci. Lett.* 187, 245–258.
- Froger, J.L., Fukushima, Y., Briole, P., Staudacher, T., Souriot, T., Villeneuve, N., 2004. The deformation field of the August 2003 eruption at Piton de la Fournaise, Reunion Island, mapped by ASAR interferometry. *Geophys. Res. Lett.* 31. <http://dx.doi.org/10.1029/2004GL020479>.
- Froger, J.L., Famin, V., Cayol, V., Augier, A., Michon, L., Lénat, J.F., 2015. Time-dependent displacements during and after the April 2007 eruption of Piton de la Fournaise, revealed by interferometric data. *J. Volcanol. Geotherm. Res.* 296:55–68. <http://dx.doi.org/10.1016/j.jvolgeores.2015.02.014>.
- Fukushima, Y., Cayol, V., Durand, P., 2005. Finding realistic dike models from interferometric synthetic aperture radar data: the February 2000 eruption at Piton de la Fournaise. *J. Geophys. Res.* 110, B03206. <http://dx.doi.org/10.1029/2004JB003268>.
- Fukushima, Y., Cayol, V., Durand, P., Massonnet, D., 2010. Evolution of magma conduits during the 1998–2000 eruptions of Piton de la Fournaise volcano, Réunion Island. *J. Geophys. Res.* <http://dx.doi.org/10.1029/2009JB007023>.
- Got, J.L., Peltier, A., Staudacher, T., Kowalski, P., Boissier, P., 2013. Edifice strength and magma transfer modulation at Piton de la Fournaise volcano. *J. Geophys. Res.* 118: 1–18. <http://dx.doi.org/10.1002/jgrb.50350>.
- Grandin, R., Socquet, A., Binet, R., Klinger, Y., Jacques, E., de Chabalière, J.B., King, G.C.P., Lasserre, C., Tait, S., Tapponnier, P., Delorme, A., Pinzuti, P., 2009. September 2005 Manda Hararo-Dabbahu rifting event. Afar (Ethiopia): Constraints provided by geodetic data. *J. Geophys. Res. Solid Earth* 114. <http://dx.doi.org/10.1029/2008JB005843>.
- Grandin, R., Klein, E., Métois, M., Vigny, C., 2016. Three-dimensional displacement field of the 2015 Mw8.3 Illapel earthquake (Chile) from across- and along-track Sentinel-1 TOPS interferometry. *Geophys. Res. Lett.* 43, 2552–2561.
- Hanssen, R. (Ed.), 2001. *Radar Interferometry, Data Interpretation and Error Analysis*. Kluwer Academic Publishers, p. 308.
- Herring, T.A., King, R.W., McClusky, S.C., 2010. *GAMIT: GPS Analysis at MIT*. Release 10.4. Massachusetts Institute of Technology, Cambridge.
- Houlié, N., Briole, P., Bonforte, A., Puglisi, G., 2006. Large scale ground deformation of Etna observed by GPS between 1994 and 2001. *Geophys. Res. Lett.* 33 (2). <http://dx.doi.org/10.1029/2005GL024414>.
- Jaggard, T.A., Finch, R.H., 1929. Tilt records for thirteen years at the Hawaiian Volcano Observatory. *Seismol. Soc. Am. Bull.* 19 (1), 38–51.
- Jonsson, S., 2009. Stress interaction between magma accumulation and trapdoor faulting on Sierra Negra volcano, Galapagos. *Tectonophysics* 471 (1–2), 36–44.
- Jonsson, S., Zebker, H., Cervelli, P., Segall, P., Garbeil, H., Mouginiis-Mark, P., Rowland, S., 1999. A shallow-dipping dike fed the 1995 flank eruption at Fernandina Volcano, Galapagos, observed by satellite radar interferometry. *Geophys. Res. Lett.* 26, 1077–1080.
- Jung, H.S., Won, J.S., Kim, S.W., 2009. An improvement of the performance of multiple aperture SAR interferometry (MAI). *IEEE Trans. Geosci. Remote Sens.* 47:2859–2869. <http://dx.doi.org/10.1109/TGRS.2009.2016554>.
- Li, Z., Fielding, E.J., Cross, P., Muller, J.-P., 2006. Interferometric synthetic aperture radar atmospheric correction: GPS topography-dependent turbulence model. *J. Geophys. Res.* 111, B02404. <http://dx.doi.org/10.1029/2005JB003711>.
- Lin, Y.N., Simons, M., Hetland, E.A., Muse, P., DiCaprio, C., 2010. A multiscale approach to estimating topographically correlated propagation delays in radar interferograms. *Geochim. Geophys. Geosyst.* 11. <http://dx.doi.org/10.1029/2010GC003228>.
- Massonnet, D., Feigl, K.L., 1998. Radar interferometry and its application to changes in the Earth's surface. *Rev. Geophys.* 36 (4), 441–500.
- Massonnet, D., Rossi, M., Carmona, C., Adragna, F., Peltzer, G., Feigl, K., Rabaut, T., 1993. The displacement field of the Landers earthquake mapped by radar interferometry. *Nature* 364, 138–142.
- Owen, S., Segall, P., Lisowski, M., Miklius, A., Muray, M., Bevis, M., Foster, J., 2000. January 30, 1997 eruptive event on Kilauea Volcano, Hawaii, as monitored by continuous GPS. *Geophys. Res. Lett.* 27 (17), 2757–2760.
- Palano, M., Puglisi, G., Gresta, S., 2008. Ground deformation patterns at Mt. Etna from 1993 to 2000 from joint use of InSAR and GPS techniques. *J. Volcanol. Geotherm. Res.* 169 (3–4), 99–120.
- Parks, M.M., Moore, J.D.P., Papanikolaou, X., Biggs, J., Mather, T.A., Pyle, D.M., Raptakis, C., Paradissis, D., Hooper, A., Parsons, B., Nomikou, P., 2015. From quiescence to unrest: 20 years of satellite geodetic measurements at Santorini volcano, Greece. *J. Geophys. Res. Solid Earth* 120, 1309–1328.
- Pavez, A., Remy, D., Bonvalot, S., Diament, M., Gabalda, G., Froger, J.L., Julien, P., Legrand, D., Moisset, D., 2006. Insight into ground deformation at Lascar volcano (Chile) from SAR interferometry, photogrammetry and GPS data: implication on volcano dynamics and future space monitoring. *Remote Sens. Environ.* 100, 307–320.
- Peltier, A., Staudacher, T., Bachèlery, P., 2007. Constraints on magma transfers and structures involved in the 2003 activity at Piton de la Fournaise from displacement data. *J. Geophys. Res.* 112, B03207. <http://dx.doi.org/10.1029/2006JB004379>.
- Peltier, A., Famin, V., Bachèlery, P., Cayol, V., Fukushima, Y., Staudacher, T., 2008. Cyclic magma storages and transfers at Piton de la Fournaise volcano (La Réunion hotspot) inferred from deformation and geochemical data. *Earth Planet. Sci. Lett.* 270 (3–4), 180–188.
- Peltier, A., Bachèlery, P., Staudacher, T., 2009. Magma transfer and storage at Piton de la Fournaise (La Réunion Island) between 1972 and 2007: a review of geophysical and geochemical data. *J. Volcanol. Geotherm. Res.* 184 (1–2):93–108. <http://dx.doi.org/10.1016/j.jvolgeores.2008.12.008>.
- Peltier, A., Bianchi, M., Kaminski, E., Komorowski, J.-C., Rucci, A., Staudacher, T., 2010. PSInSAR as a new tool to monitor pre-eruptive volcano ground deformation: validation using GPS measurements on Piton de la Fournaise. *Geophys. Res. Lett.* 37, L12301. <http://dx.doi.org/10.1029/2010GL043846>.
- Peltier, A., Got, J.-L., Villeneuve, N., Boissier, P., Staudacher, T., Ferrazzini, V., Walpersdorf, A., 2015. Long-term mass transfer at Piton de la Fournaise volcano evidenced by strain distribution derived from GNSS network. *J. Geophys. Res. Solid Earth* 120 (3): 1874–1889. <http://dx.doi.org/10.1002/2014JB011738>.
- Peltier, A., Beauducel, F., Villeneuve, N., Ferrazzini, V., Di Muro, A., Aiuppa, A., Derrien, A., Jourde, K., Taisne, B., 2016. Deep fluid transfer evidenced by surface deformation during the 2014–2015 unrest at Piton de la Fournaise volcano. *J. Volcanol. Geotherm. Res.* 321:140–148. <http://dx.doi.org/10.1016/j.jvolgeores.2016.04.031>.
- Pinel, V., Hooper, A., De la Cruz-Reyna, S., Reyes-Davila, G., Doin, M.P., Bascou, P., 2011. The challenging retrieval of the displacement field from InSAR data for andesitic stratovolcanoes: case study of Popocatepetl and Colima volcano, Mexico. *J. Volcanol. Geotherm. Res.* 200, 49–61.
- Pinel, V., Poland, M.P., Hooper, A., 2014. Volcanology: lessons learned from synthetic aperture radar imagery. *J. Volcanol. Geotherm. Res.* 289:81–113. <http://dx.doi.org/10.1016/j.jvolgeores.2014.10.010>.
- Poland, M.P., Miklius, A., Sutton, A.J., Thornber, C.R., 2012. A mantle-driven surge in magma supply to Kilauea Volcano during 2003–2007. *Nat. Geosci.* 5 (4):295–300. <http://dx.doi.org/10.1038/ngeo1426>.
- Puysségur, B., Michel, R., Avouac, J.P., 2007. Tropospheric phase delay in interferometric synthetic aperture radar estimated from meteorological model and multi-spectral imagery. *J. Geophys. Res.* 112, B05419. <http://dx.doi.org/10.1029/2006JB004352>.
- Remy, D., Bonvalot, S., Briole, P., Murakami, M., 2003. Accurate measurements of tropospheric effects in volcanic areas from SAR interferometry data: application to Sakurajima volcano (Japan). *Earth Planet. Sci. Lett.* 213, 299–310.
- Remy, D., Chen, Y., Froger, J.L., Bonvalot, S., Cordoba, M., Fustos, J., 2015. Revised interpretation of recent InSAR signals observed at Llaima volcano (Chile). *Geophys. Res. Lett.* 42. <http://dx.doi.org/10.1002/2015GL063872>.
- Roult, G., Peltier, A., Taisne, B., Staudacher, T., Ferrazzini, V., Di Muro, A., the OVPF team, 2012. A new comprehensive classification of the Piton de la Fournaise activity spanning the 1985–2010 period. Search and analysis of short-term precursors from a broad-band seismological station. *J. Volcanol. Geotherm. Res.* 241–242:78–104. <http://dx.doi.org/10.1016/j.jvolgeores.2012.06.012>.
- Samsanov, S., Feng, W., Peltier, A., Geirsson, H., D'Oreye, N., Tiampo, K., 2017. Multidimensional small baseline subset (MSBAS) for volcano monitoring in two dimensions: opportunities and challenges. Case study Piton de la Fournaise volcano GSA Abstract #292818 - Cordilleran Section - 113th Annual Meeting.
- Shirzaei, M., Burgmann, R., 2012. Topography correlated atmospheric delay correction in radar interferometry using wavelet transforms. *Geophys. Res. Lett.* 39. <http://dx.doi.org/10.1029/2011GL049971>.
- Sigmundsson, F., Durand, P., Massonnet, D., 1999. Opening of an eruption fissure and seaward displacement at Piton de la Fournaise volcano measured by RADARSAT satellite radar interferometry. *Geophys. Res. Lett.* 26, 533–536.
- Sigmundsson, F., Hreinsdóttir, S., Hooper, A., Arnadóttir, T., Pedersen, R., Roberts, M.J., Oskarsson, N., Auriac, A., Decriem, J., Einarsson, P., Geirsson, H., Hensch, M., Ofeigsson, B.G., Sturkell, E., Sveinbjörnsson, H., Feigl, K.L., 2010. Inflation triggering of the 2010 Eyjafjallajökull explosive eruption. *Nature* 468, 426–430.
- Sigmundsson, F., Hooper, A., Hreinsdóttir, S., Vogfjörð, K.S., Ofeigsson, B.G., Heimisson, E.R., Dumont, S., Parks, M., Spaans, K., Gudmundsson, G.B., Drouin, V., Arnadóttir, T., Jónsdóttir, K., Gudmundsson, M.T., Högnadóttir, T., Fridriksdóttir, H.M., Hensch, M., Einarsson, P., Magnússon, E., Samsanov, S., Brandsdóttir, B., White, R.S., Agustsdóttir, T., Greenfield, T., Gree, R.C., Rut Hjartardóttir, A.R., Pedersen, R., Bennett, R.A., Geirsson, H., La Femina, P.C., Björnsson, H., Pálsson, F., Sturkell, E., Bean, C.J., Möllhoff, M., Braiden, A.K., Eibl, E.P.S., 2015. Segmented lateral dyke growth in a rifting event at Bar [eth] arbunga volcanic system, Iceland. *Nature* 517, 191–195.
- Staudacher, T., Peltier, A., 2016. Ground deformation at Piton de la Fournaise (La Réunion Island), a review from 20 years of GNSS monitoring. In: Bachèlery, P., Lénat, J.F., Di Muro, A., Michon, L. (Eds.), *Active Volcanoes of the Southwest Indian Ocean: Piton de la Fournaise and Karthala*. Active volcanoes of the world. Springer, Berlin: pp. 139–170 http://dx.doi.org/10.1007/978-3-642-31395-0_9.
- Strang, G., 1986. *Introduction to Applied Mathematics*. Wellesley-Cambridge (758 pp. ISBN 0-9614088-0-4).
- Strang, G., Borre, K., 1997. *Linear Algebra, Geodesy, and GPS*. Wellesley-Cambridge Press, Wellesley MA, USA (640 pp.).
- Sudhaus, H., Jonsson, S., 2009. Improved source modeling through combined use of InSAR and GPS under consideration of correlated data errors: application to the June 2000 Kleifarvatn earthquake, Iceland. *Geophys. J. Int.* 176, 389–404.
- Toutain, J.-P., Bachèlery, P., Blum, P.-A., Cheminee, J.L., Delorme, H., Fontaine, L., Kowalski, P., Tauchy, P., 1992. Real time monitoring of vertical ground deformations during eruptions at Piton de la Fournaise. *Geophys. Res. Lett.* 19 (6), 553–556.
- Villeneuve, N., Bachèlery, P., 2006. Revue de la typologie des éruptions au Piton de la Fournaise, processus et risques volcaniques associés. (Cybergeo: European Journal of Geography, Environment, Nature, Paysage 336, URL). <http://cybergeo.revues.org/index2536.html>.
- Wadge, G., Webley, P.W., James, I.N., Bingley, R., Dodson, A., Waugh, S., Veneboer, T., Puglisi, G., Mattia, M., Baker, D., Edwards, S.C., Edwards, S.J., Clarke, P.J., 2002. Atmospheric models, GPS and InSAR measurements of the tropospheric water vapour field over Mount Etna. *Geophys. Res. Lett.* 29 (19), 11-1–11-4.

- Wauthier, C., Oyen, A.M., Marinkovic, P.S., Cayol, V., Gonzalez, J.P., Hanssen, R.F., Walter, T.R., 2009. L-band and c-band InSAR studies of African volcanic areas. *Geoscience and Remote Sensing Symposium, 2009 IEEE International, IGARSS 2009*, 12–17 July 2009, Cape Town, South Africa, 2, II-210. IEEE (July).
- Webley, P.W., Bingley, R.M., Dodson, A.H., Wadge, G., Waugh, S.J., James, I.N., 2002. Atmospheric water vapour correction to InSAR surface motion measurements on mountains: results from a dense GPS network on Mount Etna. *Phys. Chem. Earth, Parts A/B/C* 27 (4–5), 363–370.
- Wilson, R.M., 1935. *Ground Surface Movements at Kilauea Volcano, Hawaii*: Honolulu, University of Hawai'i Research Publication 10 (56 pp.).
- Wright, T.J., Parsons, B.E., Lu, Z., 2004. Toward mapping surface deformation in three dimensions using InSAR. *Geophys. Res. Lett.* 31, L01607. <http://dx.doi.org/10.1029/2003GL018827>.
- Wright, T., Ebinger, C., Biggs, J., Ayele, A., Yirgu, G., Keir, D., Stork, A., 2006. Magma-maintained rift segmentation at continental rupture in the 2005 Afar dyking episode. *Nature*:442 <http://dx.doi.org/10.1038/nature04978>.
- Yun, S., Segall, P., Zebker, H., 2006. Constraints on magma chamber geometry at Sierra Negra Volcano, Galápagos Islands, based on InSAR observations. *J. Volcanol. Geotherm. Res.* 150, 232–243.
- Zebker, H.A., Rosen, P.A., Hensley, S., 1997. Atmospheric effects in interferometric synthetic aperture radar surface deformation and topographic maps. *J. Geophys. Res. Solid Earth* 102 (7), 547–7,563.